nanomaterials

Article

Effect of the Nature of the Electrolyte on the Behavior of Supercapacitors Based on Transparent $ZnMn_2O_4$ Thin Films

Juan José Peinado-Pérez [1], Maria Cruz López-Escalante [2] and Francisco Martín [2,*]

[1] Department of Applied Physics I, Faculty of Sciences, University of Málaga, Campus de Teatinos, E-29071 Málaga, Spain; q12pepej@uma.es
[2] Department of Chemical Engineering, Faculty of Sciences, University of Málaga, Campus de Teatinos, E-29071 Málaga, Spain; mclopez@uma.es
* Correspondence: marjim@uma.es

Abstract: Transparent $ZnMn_2O_4$ thin films on indium tin oxide (ITO) were prepared through spray pyrolysis and implemented as electrodes in symmetric supercapacitors (SSCs). A specific capacitance value of 752 F g^{-1} at 0.5 A g^{-1} and a 70% retention over 3000 galvanostatic charge–discharge (GCD) cycles were reached with a 1.0 M Na_2SO_4 electrolyte in a three-electrode electrochemical cell. Analysis of the cycled electrodes with 1.0 M Na_2SO_4 revealed a local loss of electrode material; this loss increases when electrodes are used in SCCs. To avoid this drawback, solid polyvinylpyrrolidone-$LiClO_4$ (PVP-$LiClO_4$) and quasi-solid polyvinylpyrrolidone-ionic liquid (PVP-ionic liquid) electrolytes were tested in SSCs as substitutes for aqueous Na_2SO_4. An improvement in capacitance retention without a loss of electrode material was observed for the PVP-ionic liquid and PVP-$LiClO_4$ electrolytes. With these non-aqueous electrolytes, the tetragonal structure of the $ZnMn_2O_4$ spinel was maintained throughout the cyclic voltammetry (CV) cycles, although changes occurred in the stoichiometry from $ZnMn_2O_4$ to Mn-rich $Zn_{1-x}Mn_{3-x}O_4$. In the case of the electrolyte 1.0 M Na_2SO_4, the loss of Zn^{2+} led to the formation of MnO_2 via $Zn_{1-x}M_{3-x}O_4$. The location of the three SCCs in the Ragone plot shows supercapacitor behavior. The electrochemical results prove that the pseudocapacitance is the major contributor to the electrode capacitance, and the SCCs can therefore be considered as pseudocapacitors.

Keywords: energy storage; supercapacitor; $ZnMn_2O_4$; thin film; electrolyte; transparent

check for updates

Citation: Peinado-Pérez, J.J.; López-Escalante, M.C.; Martín, F. Effect of the Nature of the Electrolyte on the Behavior of Supercapacitors Based on Transparent $ZnMn_2O_4$ Thin Films. *Nanomaterials* **2023**, *13*, 3017. https://doi.org/10.3390/nano13233017

Academic Editors: Huiyu Chen and Xiaodong Tian

Received: 28 October 2023
Revised: 21 November 2023
Accepted: 22 November 2023
Published: 24 November 2023

1. Introduction

There are currently several active approaches to promote the development of storage systems, as well as generation and storage together, to overcome the inherent seasonality of renewable energies. There are many devices that can store electric energy, such as rechargeable lithium-ion batteries, capacitors, electrochemical capacitors, and fuel cells. They all differ in their energy density, power density, efficiency, voltage window, and current density [1]. Electrochemical capacitors, also named supercapacitors (SCs), are devices with a promising future as energy storage systems because, compared to other systems, they offer a high power density, fast charge–discharge rate, excellent cycle stability, and low cost and they can be designed as eco-friendly systems with the proper selection of materials [2,3]. There is an emerging demand for transparent optoelectronic devices where transparent supercapacitors with high optical transmittance, but without sacrificing performance, will be needed.

The energy storage mechanism of SCs is due to the double-layer capacitance formed by the electrode–electrolyte interface and faradaic processes produced by reversible adsorption–desorption or oxidation–reduction chemical reactions (pseudocapacitance) [4]. SCs' electrochemical performance is closely related to the electrode material, surface area, porosity, electrochemical activity, and kinetic characteristics of the electrodes [5]. Therefore, this implies that, in addition to being a suitable material selection, it is important to improve the ion and electron transport of the electrode, and the electrode/electrolyte interface [4,6,7].

Carbon-based materials, conducting polymers, and metal oxides are used as electrode materials. These materials have advantages and disadvantages. Carbon materials show great mechanical strength, excellent electronic conductivity, high specific surface area accessible to the electrolyte ions, and can be obtained from biomass [8,9]. Graphene oxide tends to aggregate and restack, making its surface less accessible to the electrolyte. Conducting polymers have a relatively high conductivity and capacitance compared to carbon-based electrode materials [10]. However, reduction–oxidation causes mechanical stress in conducting polymers, limiting their stability during charge–discharge cycles. Metal oxides, such as MnO_2, exhibit high energy and power density. However, they suffer from poor electrical conductivity, capacitance fading, short cycling lifetime due to their intrinsic drawbacks of crystallographic instability, volume expansion, and severe aggregation during redox reactions [11]. Zhong-Shuai et al. [12] comparatively reported the pros and cons of graphene, metal oxides, and graphene/metal oxide composites.

Manganese oxide-based materials are interesting for SCs due to their high theoretical specific capacitance, excellent capacitive performance in aqueous electrolytes [13,14], multivalence, low cost, and environmental friendliness. Manganese can adopt ten oxidation states, 7+ through 3−, but only three oxidation states, 2+, 3+, and 4+, are usually observed [15,16]. Manganese forms numerous stable stoichiometric oxides (MnO_2, Mn_2O_3, Mn_3O_4, and MnO) and metastable oxides (such as Mn_5O_8) in which Mn^{2+} and Mn^{3+} coexist [17]. Manganese oxides form a variety of polymorphs; for example, MnO_2 may exist as crystalline α, β, γ, δ or ε and the oxyhydroxide MnOOH exhibits three natural polymorphisms (α, β, γ).

Manganese oxide MnO_2 has a large theoretical specific capacitance of 1370 F g^{-1}, but its high resistivity (10^{-6} S cm^{-1}) reduces electronic conductivity substantially [18]. Electrodes with MnO_2 as the principal active material suffer from a short cycle life, mainly due to Mn loss from the electrode through the disproportionation reaction to the production of soluble Mn^{2+} [2,19–21]. In order to avoid or reduce this unwanted behavior, some authors chose to limit the potential window to 0.1–1.0 V, reducing the probability of a MnO_2 disproportion reaction [2], while other authors have tried to introduce different elements in the electrode matrix in order to increase its conductivity [19]. Reversible Zn^{2+} intercalation/deintercalation in the MnO_2 host framework and the formation of $ZnMn_2O_4$ combined with H^+ co-intercalation are recognized as the main energy storage mechanisms in Zn/MnO_2 cells [22].

Aqueous Zn ion batteries adopt the controlled chemical extraction/insertion of Zn [23]. Zn forms, with Mn, various compounds ranging from mixed oxides to spinel compounds such as $ZnMn_2O_4$. $ZnMn_2O_4$ belongs to the AB_2O_4 spinel family, with Zn^{2+} and Mn^{3+} ions at the center of tetrahedral and octahedral sites, respectively, while the oxygen atoms are distributed over the corners of the octahedra and tetrahedra [24,25]. The Zn^{2+} in the spinel $ZnMn_2O_4$ can be replaced by divalent ions (Cd^{2+}, Ca^{2+}, Mg^{2+}, Mn^{2+}), while Mn^{3+} can be replaced by trivalent ions (Al^{3+}, Fe^{3+}) [26]. However, the substitution of Zn^{2+} by Mn^{2+} would be compensated by the simultaneous oxidation of Mn^{3+} to Mn^{4+}, which is described by the formula t-[Zn^{2+}, Mn^{2+}] o-[Mn^{3+}, Mn^{4+}, Zn^{2+}]$_2$ $[O]_4$ (t, o, for tetrahedral and octahedral sites, respectively) [24]. Mn-rich spinels, such as $Zn_xMn_{3-x}O_4$ with $x < 1$, are stable at low temperatures [24]. $Zn_xMn_{3-x}O_4$ tetragonal spinel structures were found at room temperatures for a range of values of x from 0 to 1 [27]. With $x > 1$, Peitado et al. found a mixture of tetragonal and hexagonal spinel structures at high temperature [28]. $ZnMn_2O_4$ has been proposed as an anode for Li-ion batteries [29,30] and as electrodes for supercapacitors [31].

In this work, we analyzed the effect of an electrolyte on the spinel $ZnMn_2O_4$ when it is used as an electrode in symmetric SCs. Analysis of the cycled electrodes shows that with Na_2SO_4 aqueous electrolytes, irreversible zinc extraction and the local loss of electrode material occur. To avoid this drawback, quasi-solid PVP-ionic liquid and solid

PVP-$LiClO_4$ electrolytes were tested as substitutes for aqueous Na_2SO_4 in symmetric supercapacitors (SSCs). During CV cycles, the tetragonal spinel $ZnMn_2O_4$ undergoes a change in stoichiometry through the loss of Zn to Mn-rich phases, with $Zn_{1-x}Mn_{3-x}O_4$ maintaining a tetragonal structure until it finally becomes MnO_2, as is the case with the 1.0 M Na_2SO_4 electrolyte. This process is inhibited to a greater or lesser extent by the PVP-ionic liquid and PVP-$LiClO_4$ electrolytes, resulting, after CV cycles, in a gradient of different stoichiometries in the composition of the thin film from Na_2SO_4 to $Zn_{0.67}Mn_{2.33}O_4$.

2. Materials and Methods

2.1. Preparation of $ZnMn_2O_4$ Electrodes

$ZnMn_2O_4$ electrodes were prepared through spray pyrolysis over commercial In_2O_3:Sn (ITO) glass (XOPGlass, Castellón, Spain). In this deposition method, the precursor solution was pushed through a syringe pump into the spray nozzle to be nebulized on the substrate with a stream of compressed air. The substrate was kept at a controlled temperature. The precursors zinc acetate ($Zn(AC)_2{\cdot}2H_2O$) and manganese acetate ($Mn(AC)_2{\cdot}4H_2O$) (Sigma-Aldrich, St. Louis, MO, USA) were dissolved in distilled water with concentrations of 0.005 M and 0.01 M, respectively. Regarding the experimental conditions of spray pyrolysis, the flow rate and substrate temperature were set at the values of 20 mL h^{-1} and 400 °C, respectively, while the deposition time varied from 2 to 15 min. The electrode size was 2.5 cm × 4.0 cm.

2.2. Supercapacitor Assembly

Three symmetric supercapacitors (SSCs) were assembled using two $ZnMn_2O_4$/ITO/glass electrodes and three different electrolytes (Figure 1). The first electrolyte was prepared using an acetate film soaked in 1.0 M Na_2SO_4 (Sigma-Aldrich, St. Louis, MO, USA) (Figure 1a); the second with 6.0 g of $LiClO_4$ (Sigma-Aldrich, St. Louis, MO, USA) and 6.0 g of polyvinyl pyrrolidone (PVP) (Mw:1,300,000) (Sigma-Aldrich, St. Louis, MO, USA) dissolved in 75.0 mL of ethanol (Panreac Quimica, Barcelona, Spain) (named as PVP-$LiClO_4$). This solution was screen-printed onto the ITO substrate and dried (Figure 1b). The ionic conductivity of the solid electrolyte obtained was 1.89 10^{-4} S cm^{-1}; however, this conductivity may decrease due to the loss of residual ethanol from the electrolyte [32]. The third electrolyte was prepared with 9.0 g of commercial ionic liquid, 1-(2-hydroxyethyl)-3-methylimidazolium tetrafluoroborate [HEMIm][BF_4] (Io-li-tec, Heilbronn, Germany), together with 16.0 g of PVP (named PVP-ionic liquid) dissolved in 55 mL of methanol. [HEMIm][BF_4] ion gel exhibits an electrochemical stability window of, ca., 5.0 V and an ionic conductivity of 5.7 10^{-3} S cm^{-1} at room temperature [33]. A 25 μm Meltonix film (Solaronix, Aubonne, Switzerland) was used to prevent the direct contact between electrodes (Figure 1b). A Meltonix polymer was also used to seal the SSCs by heating it to 60 °C. The electrode available area in the SSC_S was 2 × 2 cm^2. The PVP-ionic liquid and PVP-$LiClO_4$ electrolytes had a pH of about 6, and the pH of the aqueous electrolyte 1.0 M Na_2SO_4 was 6.2.

2.3. Characterization Methods

The thin-film crystalline structure was examined using an X-ray EMPYREAN diffractometer (PANanalytical, Malvern, UK). X-ray diffraction (XRD) spectra were recorded in the theta-theta transmission configuration, placing the sample between two Kapton foils, and by using a focusing mirror and the PIXcel 3D detector (working in 1D mode) with a step size of 0.013° (2θ). The diffractograms were recorded between 10° and 80° in 2θ with a total measuring time of 60 min. The morphology of the electrodes was studied using a field emission scanning electron microscope (FE-SEM), Helios Nanolab 650 dual beam instrument (Thermo Fisher Scientific, Waltham, MA, USA). High-resolution transmission electron microscopy (HRTEM) images and energy-dispersive X-ray spectroscopy (EDS) images were obtained on Talos F200X equipment (Thermo Fisher Scientific, Waltham, MA, USA). Optical transmittance measurements were carried out using a Varian Cary 5000 model spectrophotometer (Agilent, Santa Clara, CA, USA) with an integrating Spectralon sphere. X-ray photoelectron spectra (XPS) were recorded on a Physical Electronics PHI 5700 spectrometer (Physical Electronic, Chanhassen, MN, USA) using monochromatic Mg radiation. Adventitious C1s at 284.8 eV was used for charge shift correction.

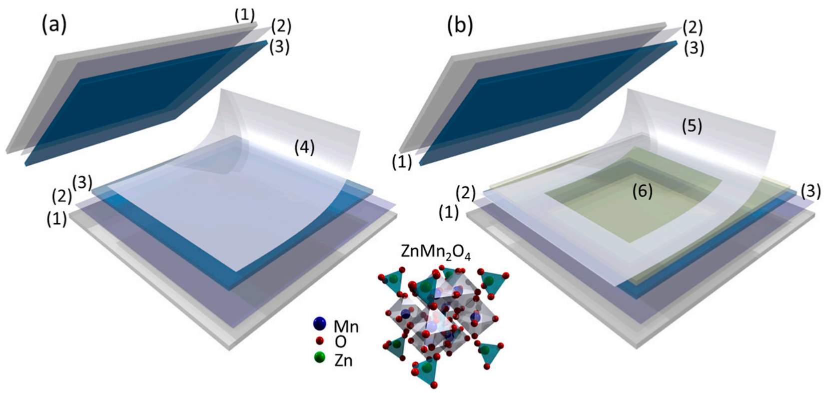

Figure 1. Scheme of the symmetric supercapacitors (**a**) using an acetate membrane soaked in 1.0 M Na_2SO_4 aqueous solution, and (**b**) with a Meltonix separation polymer and electrolyte formed by PVP- ionic liquid or PVP- $LiClO_4$. (1) Glass, (2) ITO, (3) $ZnMn_2O_4$, (4) acetate membrane soaked with 1.0 M Na_2SO_4, (5) separation polymer (frame), (6) non-aqueous electrolyte (PVP-ionic liquid or PVP-$LiClO_4$).

2.4. Electrochemical Measurements

Electrochemical performance of $ZnMn_2O_4$/ITO electrode was measured in a typical three-electrode electrochemical cell with a saturated calomel electrode (SCE) as reference electrode and platinum as counter-electrode with 1.0 M Na_2SO_4 solution as electrolyte. The electrochemical properties were investigated through cyclic voltammetry (CV), galvanostatic charge–discharge (GCD), and electrochemical impedance spectroscopy (EIS). These electrochemical measurements were carried out on a Biologic VSP potentiostat (Biologic, Knoxville, TN, USA). Due to the gel-like nature of the PVP-ionic liquid and quasi-solid nature of the PVP-$LiClO_4$ electrolytes, it was not possible to perform electrochemical tests in a three-electrode electrochemical cell. The electrochemical characterization of the SSCs was carried out with a two-electrode configuration for the three electrolytes tested. The specific capacitance C of the CVs and the GCD discharge curve ($F{\cdot}g^{-1}$), energy density E ($Wh{\cdot}kg^{-1}$), power density P ($W{\cdot}kg^{-1}$), and Coulombic efficiency η (%) were calculated according to Equations (1)–(5):

$$C = \frac{\int i(u)du}{m{\cdot}v{\cdot}\Delta V} \tag{1}$$

$$C = \frac{I{\cdot}\Delta t}{m{\cdot}\Delta V} \tag{2}$$

$$E = \frac{0.5{\cdot}\ C{\cdot}\ \Delta V^2}{3.6} \tag{3}$$

$$P = \frac{E}{\Delta t}{\cdot}3600 \tag{4}$$

$$\eta = \frac{t_d}{t_c}{\cdot}100 \tag{5}$$

where $i(u)$ is the voltammetric current (A), m is the mass of active material (g), v is the potential scan rate ($V{\cdot}s^{-1}$), ΔV is the potential window of CV of the discharge curves (V), I is the applied current (A), Δt and t_d are the discharge times (s), and t_c is the charge time (s). For SSCs where both electrodes have the same capacitance, the total capacitance is half of the electrode capacitance.

3. Results and Discussion

3.1. Characterization of the $ZnMn_2O_4$ Thin-Film Electrodes Obtained

3.1.1. Chemical and Morphological Characterization

The $ZnMn_2O_4$/ITO/glass electrodes are transparent, and their light transmittance depends on the $ZnMn_2O_4$ film thickness (Figure 2a), which is a function of the deposition time (Figure 1a). Table S1 shows the optical parameters of the thin films. The importance of the electronic conductivity of the $ZnMn_2O_4$ electrode on the specific capacitance was indicated by Zhao et al. [29]. The sheet resistance of the ITO substrate, measured using the four-point probe technique (Ossila, Sheffield, UK), was 19.93 Ω per square, and that for the thin film of $ZnMn_2O_4$ was 447.97 Ω per square with a deposition time of 2 min. Thicker $ZnMn_2O_4$ films were more resistive and their specific capacitance decreased. For this reason, films with a deposition time of 2 min and a thickness of around 35 nm were selected to form the electrodes. The 2 min layer showed the best compromise between electrical conductivity, transparency, and specific capacitance.

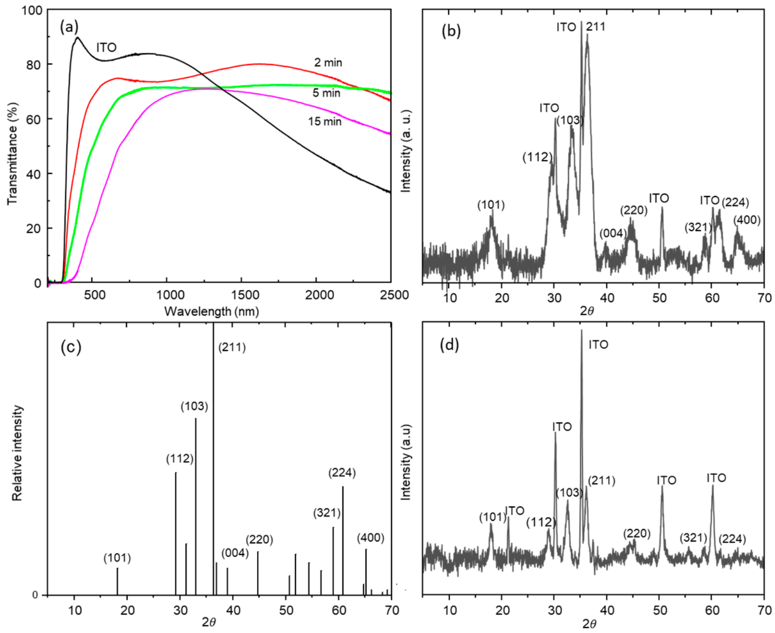

Figure 2. (**a**) Optical transmittance spectra of the $ZnMn_2O_4$/ITO/glass electrodes at different deposition times; (**b**) XRD pattern of the as-deposited electrode of $ZnMn_2O_4$ on ITO corresponding to deposition time of 15 min, (**c**) XRD standard diffraction pattern of $ZnMn_2O_4$ PDF 01-071-2499, (**d**) 5 min.

Figure 2b–d show the grazing incidence X-ray diffraction spectra of the $ZnMn_2O_4$ films with deposition times of 5 and 15 min. The $ZnMn_2O_4$ films grown with a deposition time of 2 min did not show diffraction peaks. The identified XRD peaks (Figure 2b–d) correspond to the ITO substrate and tetragonal $ZnMn_2O_4$ hetaerolite, International Centre for Diffraction Data, Power Diffraction File (PDF) 01-071-2499 (Figure 2c). No peaks of ZnO, $ZnMnO_3$, or Mn oxides were identified by XRD.

The SEM image of the $ZnMn_2O_4$ surface (Figure 3a) shows a superficial pattern of circles due to spray droplets. The chemical element surface maps using EDS (Figure 3b,c,e,f) indicate that Mn and Zn are homogeneously distributed on the surface and throughout the cross-section. Figure 3g shows an HRTEM image of the cross-section of the $ZnMn_2O_4$ thin film. Crystal planes corresponding to the most intense XRD peaks (103) (211) of the hetaerolite are indicated in the fast Fourier transform (FFT) (Figure 3i) and HRTEM images (Figure 3g,h).

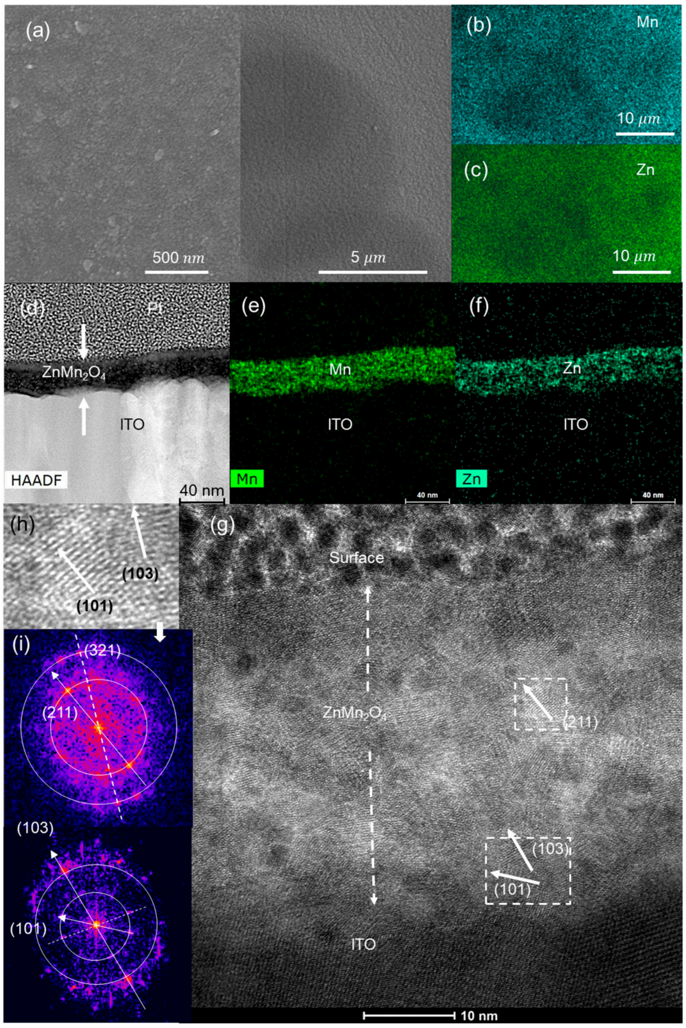

Figure 3. As-deposited $ZnMn_2O_4$ electrode: (**a**) SEM, (**b**) Mn, (**c**) Zn EDS images of the electrode surface; (**d**) HAADF; (**e**) Zn and (**f**) Mn EDS images of the electrode cross-section; (**g**) HRTEM image of the cross-section; (**h**) magnification of the marked zone; (**i**) FFTs of the film cross-section.

XPS analysis of the surface was carried out by recording the O1s, Zn2p, Zn3p, Zn LMM, Mn2p, Mn3p, and Mn3s XPS regions. Figure 4a shows the two Zn^{2+} characteristic peaks corresponding to $Zn2p_{3/2}$ and $Zn2p_{1/2}$ at binding energies of 1021.24 and 1044.34 eV, respectively, and with a spin-splitting ΔE_{Zn2p} of 23.1 eV, in agreement with the literature [34–36]. O1s was deconvoluted in two peaks (Figure 4b), at 529.5 eV, corresponding to the (Zn/Mn)–O metal bond, and at 531.2 eV for OH groups adsorbed on the surface, following the proposal of other authors [26,37,38]. The width and the asymmetry of the Mn2p core level peaks (Figure 4c) indicate the presence of manganese in at least two different oxidation states; consequently, the Mn $2p_{3/2}$ main peak was deconvoluted in two components with a ΔE_{Mn2p} splitting of 11.5 eV [26,39]: the $Mn2p_{3/2}$ main peak contribution at 641.4 eV of the Mn^{3+}, and the component at 642.4 eV attributed to Mn^{4+} [40].

The presence of Mn^{4+} in the spinel $ZnMn_2O_4$ is coherent with the findings of other authors [37,39]. Mn3s shows two multiplet split components caused by the coupling of non-ionized 3s electrons with 3d valence band electrons (Figure 4d). However, in this case, the analysis of the Mn3s is substantially more complicated because the Zn3p signal is located in the same binding energy region as Mn3s, with Zn3p multiplet split components for Zn^{2+} with values of 87.7 eV and 90.7 eV for $Zn3p_{3/2}$ and $Zn3p_{1/2}$, respectively. The magnitude of peak splitting of Mn3s (ΔE_{Mn3s}) has been reported as 5.79 eV, 5.50 eV, 5.41 eV, and 4.79 eV for MnO, Mn_3O_4, Mn_2O_3, and MnO_2, respectively [41,42]. To carry out the deconvolution of the Mn3s-Zn3p region (Figure 4d), ΔE_{Mn3s} (eV) was estimated using the equation of Beyreuther at al. (Equation (6)) [43].

$$\upsilon_{Mn} = 9.67 - 1.27\ \Delta E_{Mn3s} \quad (6)$$

where υ_{Mn} is the average oxidation state. According to the deconvolution of the Mn2p XPS signal (Figure 4c), the atomic ionic ratio Mn^{3+}/Mn^{4+} is 10.63, meaning a value of υ_{Mn} = 3.09, and ΔE_{Mn3s}= 5.18 eV (Equation (6)). This value of ΔE_{Mn3s}= 5.18 eV was used for the deconvolution of the Mn3s signal (Mn3s-Zn3p), which is shown in Figure 4d.

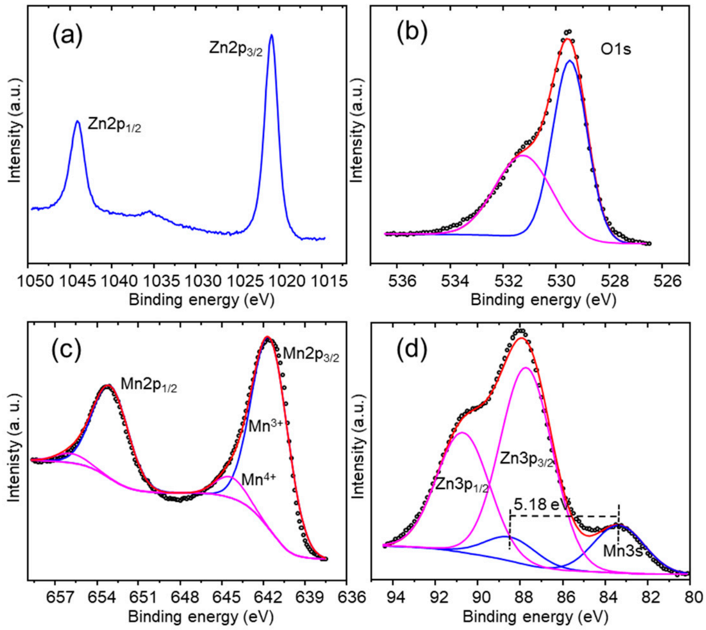

Figure 4. XPS spectra of (**a**) Zn2p, (**b**) O1s, (**c**) Mn2p, (**d**) Zn3p-Mn3s of the as-deposited $ZnMn_2O_4$ electrode.

3.1.2. Electrochemical Characterization

A three-electrode electrochemical cell with 1.0 M Na_2SO_4 aqueous solution as the electrolyte was used to characterize the behavior of the $ZnMn_2O_4$/ITO working electrode. Pt was used as the counter-electrode and a saturated calomel electrode was used as a reference. Figure 5a and Figure S1 show the cyclic voltammetry curves (CV) ranging from −0.1 to 1.2 V at different scan rates from 5 mV s^{-1} to 200 mV s^{-1}. The highest specific capacitance achieved (Equation (1)) was 697 F g^{-1} at 5 mV s^{-1}, which is better than the other values reported for $ZnMn_2O_4$ obtained through spray pyrolysis; for instance, 530 F g^{-1} at 10 mV s^{-1} was reported by Boukmouche et al. [44], and 155 F g^{-1} at 2 mV s^{-1} was reported by Guo et al. [45]. Table S2 shows, comparatively, the results obtained by other authors. The specific capacitance undergoes a progressive decrease to 187 F g^{-1} at 200 mV s^{-1} due to the diffusion limitation related to a higher potential scan rate (Figure 5b) [46–48]. The square-like shape of the CV curves is due to the contribution of the electric double-layer capacitance and the pseudocapacitance. The faradaic contribution has been reported as a non-symmetric redox process related to the reversible extraction of Zn^{2+} ions from the $ZnMn_2O_4$ spinel according to reactions described in Equations (7) and (8) [20,49–51]. The anodic peak at 0.83 V (Figure 4a) contributes to the faradaic capacitance. The shift in the anodic peak from 0.83 V to 0.94 V would be due to polarization [52]. The reported equilibrium potential of the reaction (Equation (7)) is E_{SHE}= 0.72 V (E_{SCE} = 0.961 V) [22]:

$$ZnMn_2O_4 \leftrightarrow Zn_{1-x}Mn_{3-x}O_2 + x\ Zn^{2+} + 2\ x\ e^{-} \quad (7)$$

which leads to the formation of MnO_2:

$$ZnMn_2O_4 \leftrightarrow \; 2 \; MnO_2 + Zn^{2+} + 2\,e^- \tag{8}$$

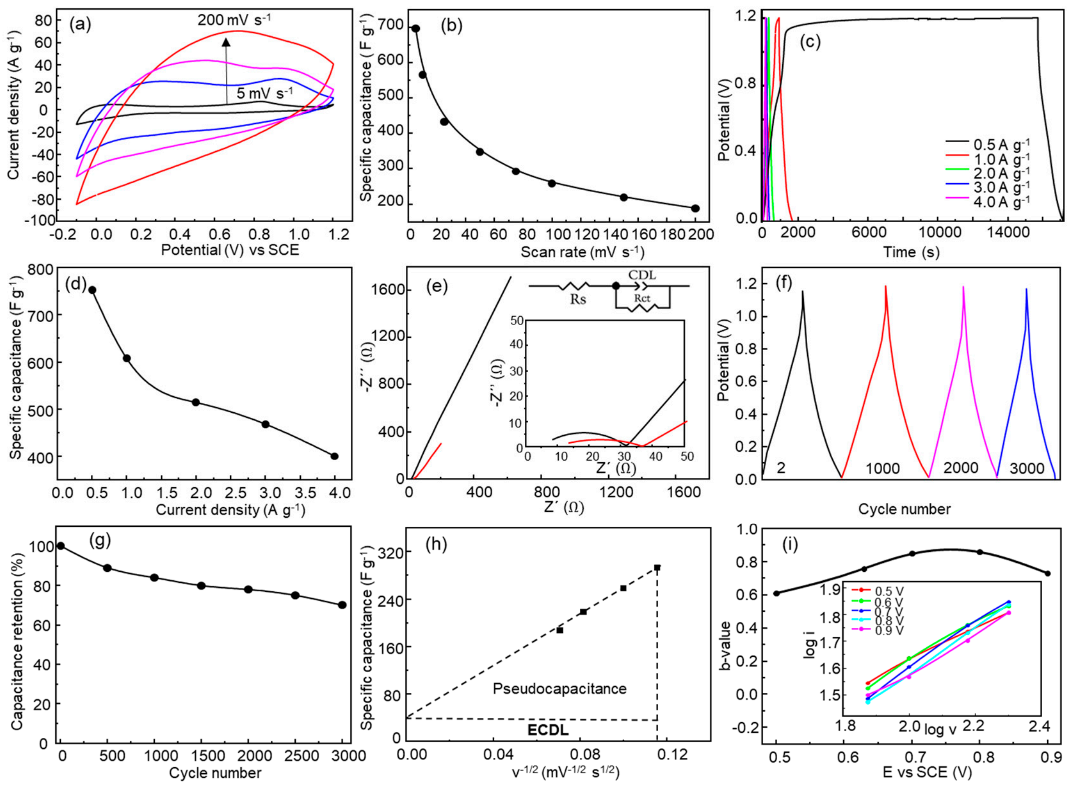

Figure 5. (**a**) Cyclic voltammetry curves of $ZnMn_2O_4$ electrode measured at different scan rates: 5, 50, 100, and 200 mV s^{-1}; (**b**) specific capacitance calculated as a function of scan rate; (**c**) GCD curves at current densities of 0.5, 1.0, 2.0, 3.0, and 4.0 A g^{-1}; (**d**) specific capacitance calculated as a function of current density; (**e**) Nyquist plot for $ZnMn_2O_4$ thin film (black: before; red: after cycling), inset: zoom of the high-frequency region (black: before; red: after CV cycles); (**f**) GCD for different number of cycles, (**g**) GCD capacitance retention; all the electrochemical analysis was carried out in 1.0 M Na_2SO_4 electrolyte; (**h**) specific capacitance vs. $v^{1/2}$; (**i**) b parameter vs. the potential, inset: log i vs. log v, v scan rate (mV s^{-1}).

The reversible intercalation/deintercalation of Zn^{2+} in the MnO_2 matrix with the formation of $ZnMn_2O_4$, shown in Equation (8), has been indicated as the main energy storage mechanism in Zn/MnO_2 batteries [22,53].

Figure 5c shows the galvanostatic charge–discharge test (GCD) with applied current densities from 0.5 A g^{-1} to 4.0 A g^{-1}. The GCD graphs present a quasi-symmetric triangular shape at higher specific current densities, 3.0 A g^{-1} and 4.0 A g^{-1}, indicating the pseudocapacitive behavior of the $ZnMn_2O_4$ electrode due to the combination of the surface capacitive reactions and the redox reactions at the electrode–electrolyte interface, following Zn^{2+} extraction/insertion. Using Equation (2), specific capacitances from 752 F g^{-1} at 0.5 A g^{-1} to 400 F g^{-1} at 4.0 A g^{-1} were obtained (Figure 5d). The specific capacitance of 752 F g^{-1} (0.5 A g^{-1}) is better than other specific capacitance values reported for electrodes based on manganese oxides obtained through spray pyrolysis, for example, with ternary compositions, such as M:Mn_3O_4, where M = Ce, Cr, Cu, and Ni were specifically reported as showing capacitances between 134 and 184 F g^{-1} at 0.5 A g^{-1}, or 460 F g^{-1} at a scan rate of 5 mV s^{-1} for Ni:Mn_3O_4 [54–57].

Electrochemical impedance spectroscopy (EIS) measurements were performed in 1.0 M Na_2SO_4 electrolytes in the 10^{-2}–10^5 Hz frequency range. Figure 5e shows the Nyquist plots for the as-deposited $ZnMn_2O_4$ electrode and after 3000 CV cycles. The impedances were simulated using the equivalent circuit shown in the inset of Figure 5e. The elements of the equivalent circuit are the solution resistance (R_s), the charge-transfer resistance (R_{ct}), and the electrochemical double-layer capacitance (EDLC). The Nyquist curves consisted of a small semicircle at high frequency for the charge–transfer resistance (R_{ct}) and a sloping line at the low-frequency region. The R_{ct} values were 25 Ω and 27 Ω for the electrode before and after CV cycles, respectively. Smaller R_{ct} is beneficial to the charge transfer. The R_s values obtained from the Nyquist plots were 7.0 Ω and 10.5 Ω for the non-cycled and cycled electrodes, respectively. Smaller values of R_s favor the diffusion of electrolyte ions [9,58].

Figure 5f shows the initial cycle and cycles with 1000, 2000, and 3000 galvanostatic charge–discharge at 2.0 A g^{-1} in a 1.0 M Na_2SO_4 electrolyte. As shown in Figure 5g, $ZnMn_2O_4$ electrodes exhibit a specific capacitance retention of 70% after 3000 GCD cycles.

The specific capacitance of the electrode is determined by the sum of the double-layer capacitance (EDLC) and the pseudocapacitance due to redox, intercalation, and diffusion processes within the active material [55–57]. The specific capacitance was plotted against the inverse of the square root of scan rate, $v^{-1/2}$ ($mV^{-1//2}$ $s^{1/2}$), to determine the contribution of EDLC and pseudocapacitance (Figure 5h) through linear fitting. At a lower CV scan rate, the plot's specific capacitance deviates from linearity and those values were excluded for the linear fitting (Figure 5h). The extrapolation of the linear fit to the y-axis assumes that the specific capacitance was expected to have an electrostatic origin [57], and the triangular area was assumed to indicate the pseudocapacitance. Therefore, from Figure 5h, it is deduced that the contribution to the specific capacitance is mainly from pseudocapacitive processes. The y-intercept of the linear fit determines the capacitance through EDLC as 24 F g^{-1} (3.4%), and the triangular area determines the capacitance provided by the pseudocapacitance as 673 F g^{-1} (96.6%), i.e., the electrode stores 96.6% of the charge based on Zn^{2+} intercalation or redox reactions and 3.4% of the charge based on the capacitive mechanism [55]. In addition, the current resulting from the voltammetric response at a specific voltage can be related to the scan rate according to the power-law formula (Equation (9)) [59]:

$$i = a\, v^b \tag{9}$$

where b is 0.5 for battery-like behavior and 1 for typical EDLC behavior [60]. The representation of log i vs. log v is shown in the inset of Figure 5i, and the values of b are shown in Figure 5i. Figure 5i shows that at the smallest potential, b approaches 0.5, indicating that the diffusion-controlled processes, and battery-like behavior, predominate. However, as the potential increases, b becomes closer to 1, indicating an increase in capacitive contributions related to non-diffusive controlled processes such as EDLC [52,61–63].

3.2. Characterization of the $ZnMn_2O_4$ Thin-Film Electrodes after Cycling Process

Chemical and Morphological Characterization

To eliminate traces of the precipitated electrolyte salt, the cycled electrodes were rinsed with water. Figure 6a shows the SEM image of the $ZnMn_2O_4$ electrode surface after 3000 CV cycles. The surface appears more textured and lacks the circular surface marks of spray droplets. This change in the surface texture is produced through chemical modification of the $ZnMn_2O_4$ according to Equations (7) and (8). The SEM-EDS images of the cycled electrode show holes corresponding to local loss of the electrode material (Figure 6a,b). The loss of Zn is also shown through EDS (Figure 6c), yielding a Mn/Zn average atomic ratio of 2 for the as-deposited electrode (Figure S2), and an average local value of 42 for the cycled electrode, with points where Zn was not detected (Figure S3). The HRTEM-EDS mapping images (Figure 6f) also show Zn loss in the cross-section of the film. The loss of electrode material is due to the solubilization of the Mn and Zn [18,49]. The Zn loss leads to irreversibility in the reactions of Equations (7) and (8), and, therefore, there is an evolution of the composition of the electrode with loss of zinc during cycling.

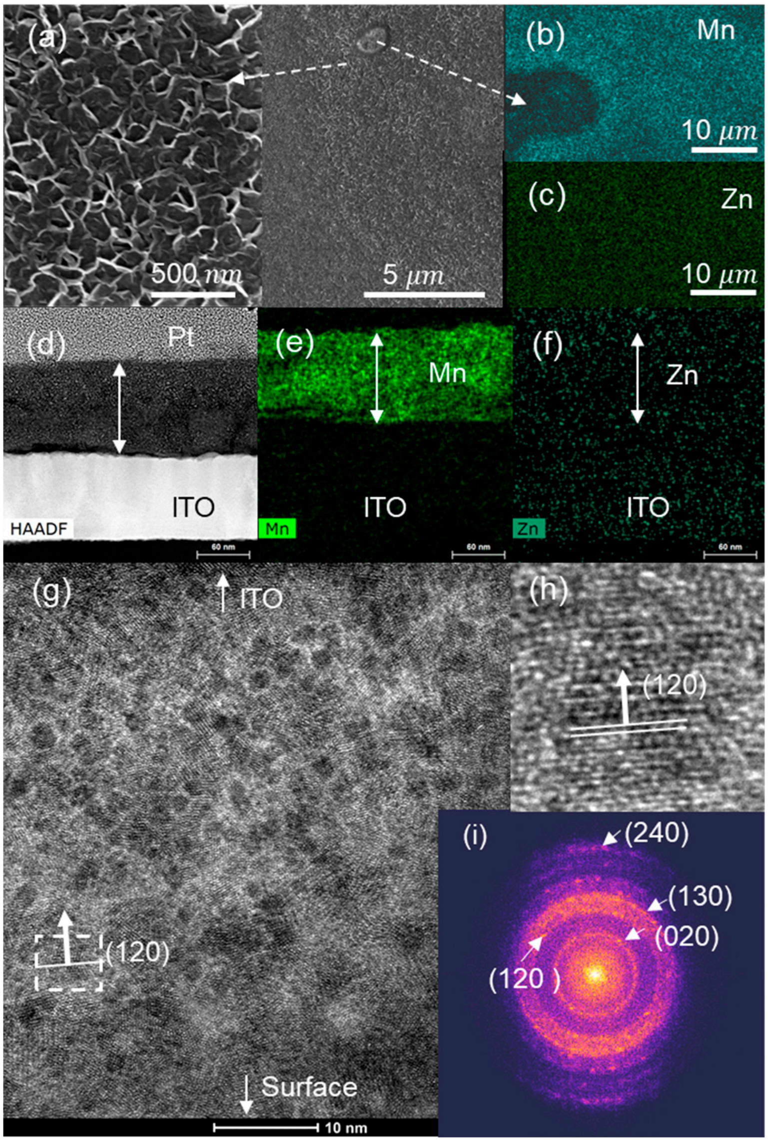

Figure 6. $ZnMn_2O_4$ electrode after 300 CV cycles: (**a**) SEM; (**b**) Mn and (**c**) Zn EDS images of the electrode surface; (**d**) HAADF; (**e**) Mn and (**f**) Zn EDS images of the electrode cross-section; (**g**) HRTEM image of the cross-section, (**h**) magnification of the marked zone; (**i**) FFTs of the film cross-section.

The XPS analysis (Figure 7a) of the electrode surface showed that after 3000 CV cycles, the intensity of the $Zn2p_{3/2}$ peak at 1021.3 eV decreased remarkably. The shift in the $Mn2p_{3/2}$ peak to a higher binding energy of 643.1eV (Figure 7c) is due to the increased contribution of the Mn^{4+} oxidation state. The Mn3s peak splitting ΔE_{Mn3s} = 4.8 eV for the cycled sample (Figure 7d), υ_{Mn}= 3.57 according to Equation (8), leading to a $MnO_{1.7}$ stoichiometry, indicates the transformation of $ZnMn_2O_4$ to MnO_2 [41], in addition to the reversible transformation of $ZnMn_2O_4$ to MnO_2. MnO_2 may participate in pseudocapacitive reactions with the electrolyte (Equations (10) and (11)):

$$\text{MnO}_2 + H^+ + e^- \leftrightarrow \text{MnOOH} \tag{10}$$

$$\text{MnO}_2 + Na^+ + e^- \leftrightarrow \text{MnOONa} \tag{11}$$

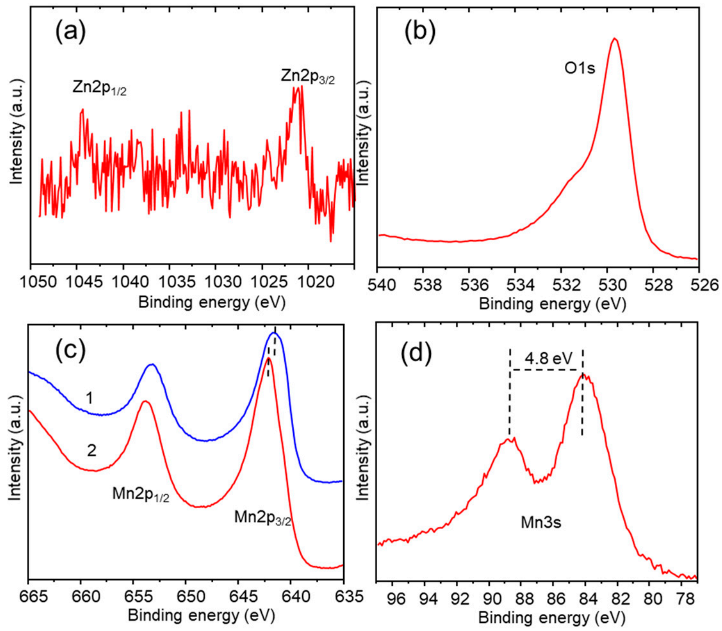

Figure 7. XPS spectra of (**a**) Zn2p, (**b**) O1s, (**c**) Mn2p, (**d**) Zn3p-Mn3s of the $ZnMn_2O_4$ electrode after 3000 CV cycles.

The formation of MnOOH was related to a better capacitive performance since it facilitates ionic exchange [64–66]. The mild-acidic condition of the aqueous Na_2SO_4 electrolyte should prevent poor cycling performance due to the formation of species such as $Mn(OH)_2$ or ZnO. However, it does not prevent dissolution of Zn^{2+}. The loss of capacitance retention during GCD cycling (Figure 5g) is a consequence of the loss of Zn and the partial dissolution of Mn in the electrolyte [22,53]. Due to film thickness and low crystallinity, it was not possible to obtain grazing XRD spectra to identify the present compounds in the electrode. However, according to the HRTEM images of the cross-section (Figure 6g,h) and the corresponding FFT (Figure 6i), interplanar distances compatible with δ-MnO_2 (PDF 04-005-4334) were obtained; these distances were also compatible with the Mn-rich spinel Zn_{1-x} $Mn_{2-y}O_4$, with values of x and y between the values of $Zn_{0.244}Mn_{2.758}O_4$ (PDF 01-070-9109) and $Zn_{0,02}Mn_{2.98}O_4$ (PDF 04-012-4910). These findings are supported by the values of the Mn/Zn ratio found through EDS (Figure S3).

3.3. Symmetrical Supercapacitor

3.3.1. 1.0 M Na_2SO_4 as Electrolyte

A symmetric supercapacitor was assembled using an acetate membrane soaked in 1.0 M Na_2SO_4 as the electrolyte (Figure 1a). Figure S4 and Figure 8a show the SSC CV curves with a potential window from $\pm$0.4 V to $\pm$1.5 V and scan rates from 25 mV s^{-1} to 200 mV s^{-1}. The specific capacitance values are shown in Table S3. The specific capacitance for $\pm$1.2 V increased from 16 F g^{-1} (200 mV s^{-1}) to 33 F g^{-1} (25 mV s^{-1}), with the highest value being 39 F g^{-1} for $\pm$1.5 V (25 mV s^{-1}). The behavior is similar to that observed for the three-electrode electrochemical cell, with an increase in current in all potential windows tested as the scan rate increases; however, the specific capacitance did not increase with an increase in scan rate. The observed drop in specific capacitance in the SC, with respect to the value measured in the three-electrode electrochemical cell, is consistent with that obtained by other authors; for example, for $NiMn_2O_4$, Sankar et al. found a drop from 202 F g^{-1} (three-electrode cell) to 50 F g^{-1} at 1 mV s^{-1} (asymmetric supercapacitor) [48].

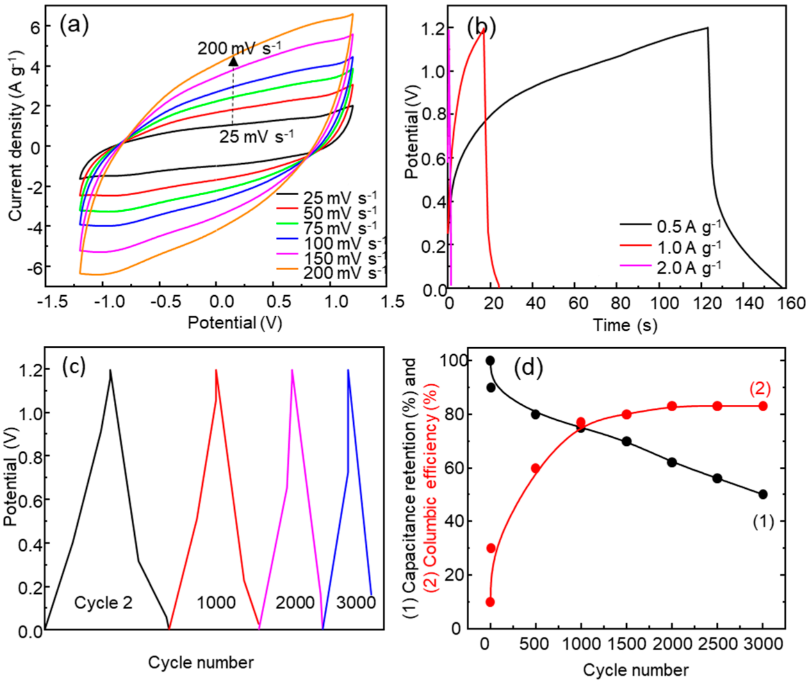

Figure 8. (**a**) Cyclic voltammetry curves with ±1.2 V potential window at scan rates from 25 to 200 mV s^{-1}; (**b**) GCD at different current densities of 0.5 A g^{-1}, 1.0 A g^{-1}, and 2.0 A g^{-1}; (**c**) GCD at cycle 2, 1000, 2000, and 3000; (**d**) capacitance retention and Coulombic efficiency (GCD cycles) for the SSC 1.0 M Na_2SO_4.

Galvanostatic charge–discharge tests were carried out at different current densities, from 0.5 A g^{-1} to 2.0 A g^{-1}, in the potential window of 0.0–1.2V (Figure 8b,c). A specific capacitance of 17 F g^{-1} was observed at a current density of 0.5 A g^{-1}, yielding an energy density of 3.4 Wh kg^{-1} and a power density of 306 W kg^{-1}, which positions this SSC as a supercapacitor in the Ragone plot. The specific capacitance values obtained from initial GCD cycles are similar and even higher than those found in the literature [21]. As the current density increases, the GCD curves show a more symmetric and triangular shape indicating better Coulombic efficiency, but the specific capacitance decreases due to the fast discharge of the supercapacitor. The electrochemical stability of the SSC was studied using 3000 GCD cycles at a current density of 1.0 A g^{-1} (Figure 8c). The SSC experienced a drop in specific capacitance as the number of GCD cycles increased (Figure 8c,d). Figure 8d shows the evolution of specific capacitance retention and Coulombic efficiency with the number of cycles. On the other hand, there was a significant loss of electrode material (Figures S3 and S9b) at the end of the 300 CV cycles as a consequence of the solubilization of Mn and Zn, as mentioned above.

3.3.2. PVP-Ionic Liquid and PVP-$LiClO_4$ as Electrolytes

Two symmetric supercapacitors were assembled using PVP-ionic liquid or PVP-$LiCLO_4$ as electrolytes following the arrangement shown in Figure 1b. The SSCs' electrochemical tests were carried out with a two-electrode configuration.

PVP-Ionic Liquid Electrolyte

Figure 9a and Figure S5 show the CV curves of the PVP-ionic liquid SSCs with potential windows from ±0.4 V to ±1.5 V and scan rates from 25 mV s^{-1} to 200 mV s^{-1}. For the two lowest potential windows of ±0.4 V and ±0.8 V, curves were obtained that were nearly rectangular and possessed a specific capacitance of 15 F g^{-1} and 23 F g^{-1}, at 25 mV s^{-1}, respectively. An increase in pseudocapacitive behavior was observed for ±1.2 V (40 F g^{-1} at 25 mV/s) and ±1.5 V (37 F g^{-1} at 25 mV s^{-1}), as shown in Table S4. The increase in the scan rate decreases the charge stored in the device due to the limitation of the diffusion processes, making the interaction between the electrolyte and the electrode material less effective. Figure 9b shows the electrochemical behavior of the device during GCD at different current densities and a potential window of 0–1.2 V. The highest specific capacitance of 15 F g^{-1} was obtained at 0.5 A g^{-1}. At lower current densities, the charge–discharge times are longer, and the GCD profile is characteristic of a supercapacitor with faradaic contribution. As the current density increases, the GCD curve adopts a more triangular profile characteristic of EDLC (Figure 9b). Through GCD, the highest energy density of 3 Wh kg^{-1} is obtained at the current density of 0.5 A g^{-1}, while the highest power density of 1080 W kg^{-1} is obtained for 2.0 A g^{-1} (Table S4). As shown in Figure 9d,e, the SSC shows good stability, maintaining a retention of 70% of its initial capacitance after 3000 GCD cycles at a current density of 1.0 A g^{-1}, and the Coulombic efficiency (Figure 6d) is higher than that obtained for SSC with 1.0 M Na_2SO_4 (Figure 5f).

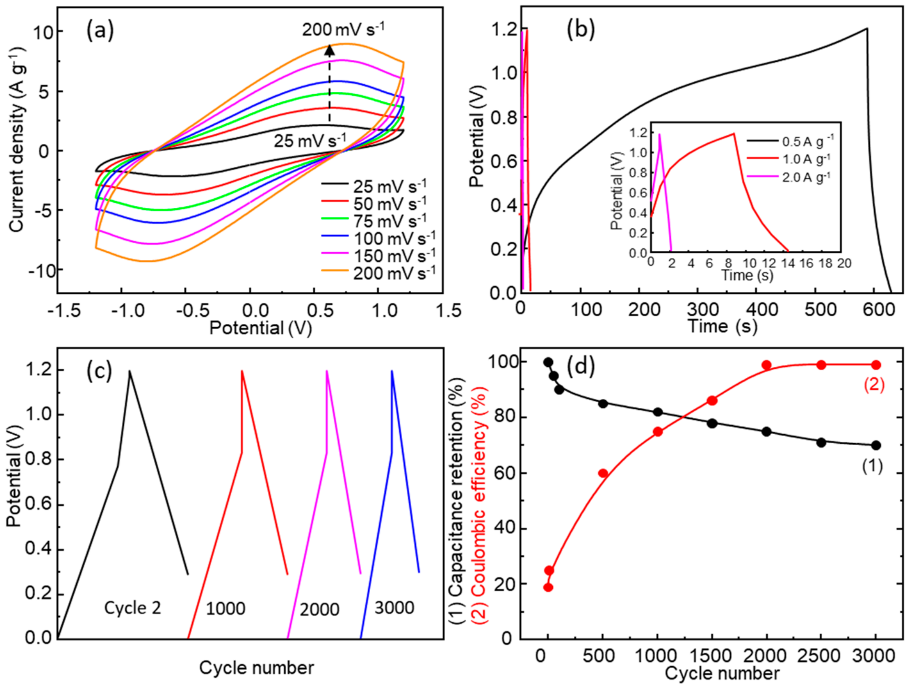

Figure 9. SCC with PVP-Ionic liquid: (**a**) CV cycles with a ±1.2 V potential window at scan rates from 25 to 200 mV s^{-1}; (**b**) GCD at current densities of 0.5 A g^{-1}, 1.0 A g^{-1}, 2.0 A g^{-1}; (**c**) GCD cycles 2, 1000, 2000, and 3000; (**d**) capacitance retention and Coulombic efficiency (GCD cycles).

After 300 CV cycles, the electrodes were recovered and washed with ethanol to remove the electrolyte on the electrode surface. The SEM image (Figure 10a) shows a more textured surface than the original electrode surface (Figure 3a), with spray droplet marks still visible after 300 CV cycles. No loss of electrode material in the form of voids is observed (Figure 10a), which may be due to a lower solubility of Zn and Mn in the PVP-ionic liquid electrolyte than in the aqueous Na_2SO_4 electrolyte, favoring the reversibility of the reactions described in Equations (7) and (8). The EDS mappings of Mn and Zn (Figure 10b–f) show that both elements are present and homogenously distributed on the surface and in the cross-section.

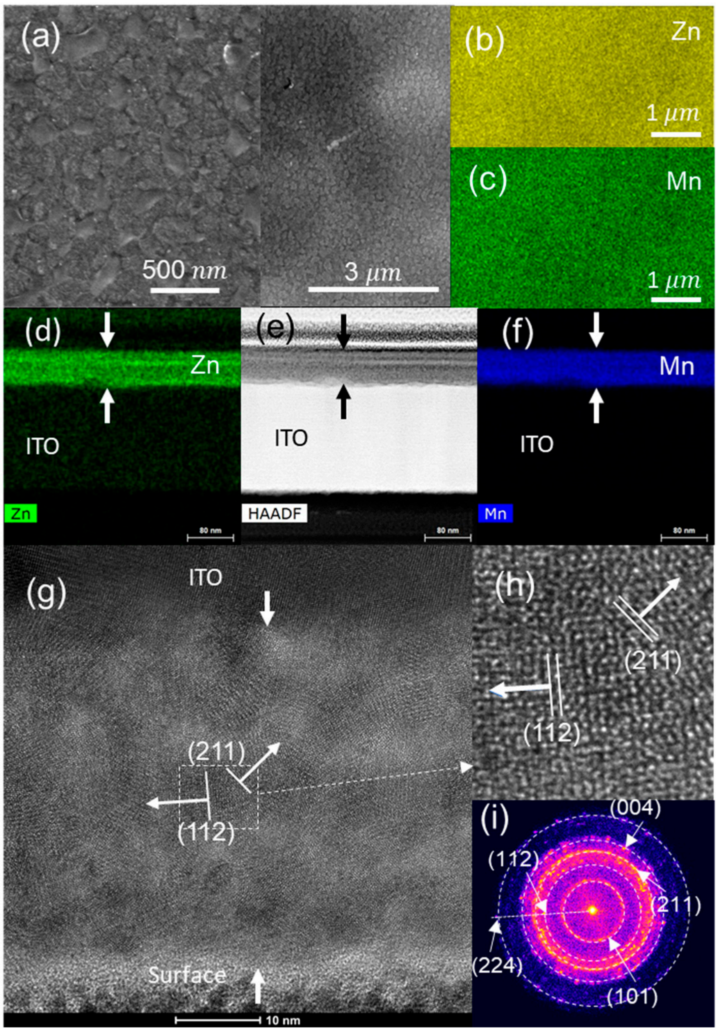

Figure 10. SCC with PVP-ionic liquid as electrolyte after 300 CV cycles: (**a**) SEM; (**b**) Zn and (**c**) Mn EDS images of the surface of the electrode; (**d**) Zn and (**f**) Mn EDS images; (**e**) HAADF images of the electrode cross-section; (**g**) HRTEM image of the cross-section; (**h**) magnification of the marked zone; (**i**) FFT of the film cross-section.

Figure 11a–d show the XPS spectra corresponding to Mn2p, Mn3s, Zn $2p_{3/2}$, and O1s. Both the Zn2p (Figure 11a) and Mn3s regions (Figure 11c) show a superficial loss of Zn, but this Zn loss is less than in the case of the Na_2SO_4 electrolyte. When the electrode was exposed to cathodic conditions at the end of the last 300th cycle of CV, the $Mn2p_{3/2}$ and Mn3s XPS peaks (Figure 11c,d) showed a shift toward lower binding energies of 640.8 eV and 82.6 eV (641.4 eV and 83.5 eV, respectively, for the as-deposited electrode), respectively, indicating the presence of Mn^{2+} [16,65,66]. This is corroborated by the deconvolution of the Mn3s-Zn3p region (Figure 11c) with ΔE_{Mn3s} = 5.8 eV for Mn3s [42,65]. FWHMs of 2.2 eV for Mn3s and 3.3 eV for Zn3p peaks were used for the deconvolution (Figure 11c). However, when the opposite electrode was analyzed using XPS at the end of the 300th CV cycle, under more oxidizing conditions, the Mn2p peak showed a shift toward higher binding energies (642.1 eV), indicating Mn^{4+} (Figure 11d).

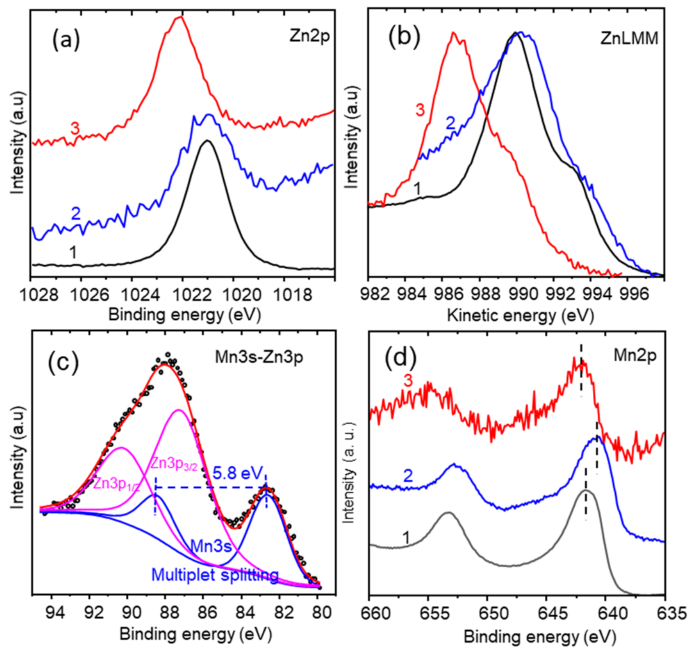

Figure 11. XPS of electrode of SCC PVP-Ionic Liquid: (**a**) Zn2p, (**b**) ZnLMM, (**c**) M3s Zn3p, (**d**) Mn2p. Electrodes: (1) as-deposited, (2) after 300 CV cycles finishing under reducing conditions, (3) after 300 cycles of CV finishing under oxidizing condition.

These XPS results are indicative of the reversibility of the redox processes occurring on both electrodes, which can deliver a more stable capacity [67]. These valence changes at the surface are compatible with the maintenance of the tetragonal structure of the spinel, t-[Zn^{2+}, Mn^{2+}]o-[Mn^{3+}, Mn^{4+}, Zn^{2+}]$_2$[O]$_4$ [24]. On the other hand, the ionic liquid is composed of imidazolium and the tetrafluoroborate anion (BF_4^-). Furthermore, the XPS Zn2p (Figure 11a) and the Auger region ZnLMM (Figure 11b) show a displacement in the binding energy to 1022 eV for $Zn2p_{3/2}$ and 986.7 eV (kinetic energy) for ZnLMM, values identified as corresponding to ZnF_2 [68]. However, in this case, these values would correspond to $Zn^{2+}[BF_4^-]$, which is proof of the chemical interaction between the electrode material and the electrolyte and is responsible for the partial solubilization of Zn in the electrode–quasi-solid-electrolyte interface. According to FFT HRTEM of the cross-section (Figure 10g–i), crystalline planes were identified that are compatible with a transformation from hetaerolite $ZnMn_2O_4$ (PDF 01-071-2499) to Mn-rich tetragonal phases such as $Zn_{0.75}Mn_{2.25}O_4$ (PDF 04-016-9607), with the stoichiometry changing across the cross-section (Figure S6). Figure S6b shows the evolution of the Mn/Zn atomic ratio in the cross-section. Figure 12 shows a scheme illustrating this transformation from $ZnMn_2O_4$ to the Mn-rich phase $Zn_{1-x}Mn_{3-x}O_4$.

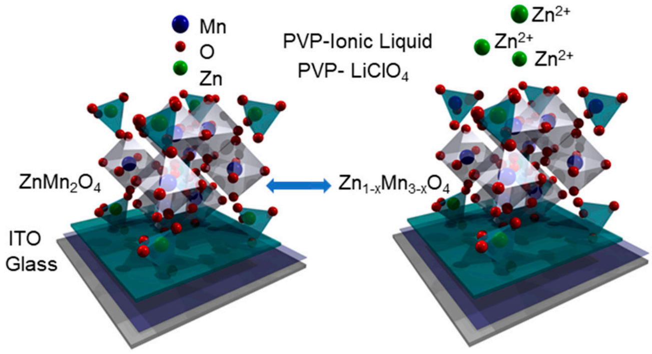

Figure 12. Scheme of the transformation from $ZnMnO_4$ to $Zn_{1-x}Mn_{3-x}O_4$.

PVP-$LiClO_4$ Electrolyte

Figure S7 and Figure 13a show the CV curves with potential windows from ±0.4 V to ±1.5 V and scan rates from 25 mV s^{-1} to 200 mV s^{-1} (Table S5). The highest CV specific capacitance value was 22 F g^{-1} for a scan rate of 25 mV s^{-1} and a potential window of ±1.2 V. Figure 13b shows the results of the GCD tests at constant current densities of 0.5 A g^{-1}, 1.0 A g^{-1}, and 2.0 A g^{-1} using a potential window of 0–1.2 V.

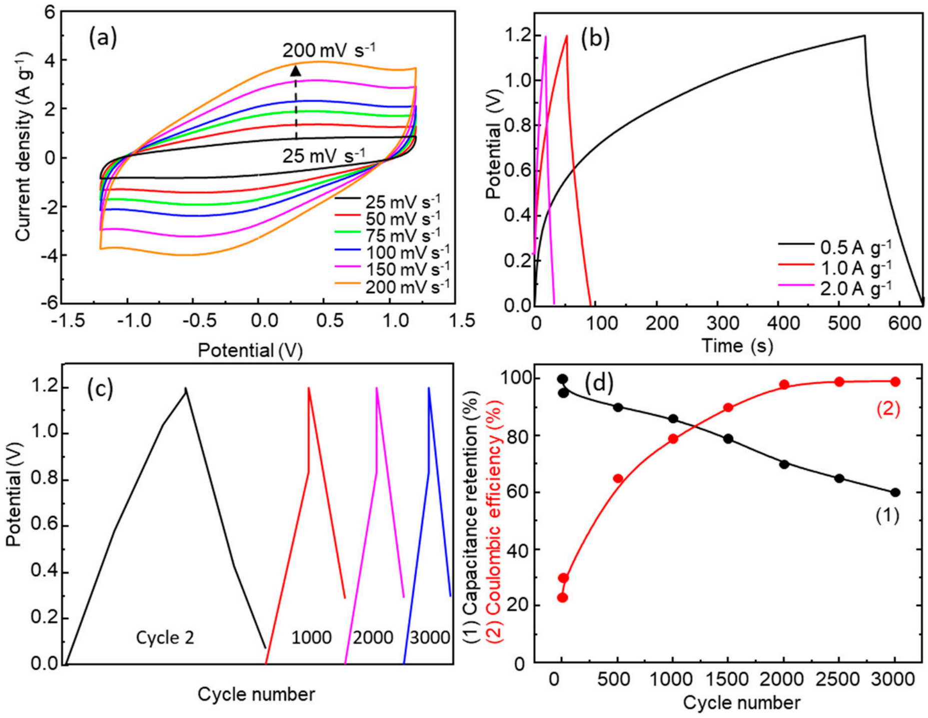

Figure 13. SCC with PVP-$LiClO_4$: (**a**) CV cycles with a ±1.2 V potential window at scan rates from 25 to 200 mV s^{-1}; (**b**) GCD at current densities of 0.5 A g^{-1}, 1.0 A g^{-1}, 2.0 A g^{-1}; (**c**) GCD cycles 2, 1000, 2000, and 3000; (**d**) capacitance retention and Coulombic efficiency (GCD cycles).

The SCC with this electrolyte shows the longest charge and discharge time of the three electrolytes. The discharge time and the specific capacitance were 94 s and 39 F g^{-1}, respectively, for an extracted current density of 0.5 A g^{-1} (Figure 13b). At higher current density, the SSC shows a reduction in discharge time and capacitance (Table S5) due to the inability of the electrolyte to sustain a high charge transfer rate. The SSC using PVP-$LiClO_4$ retained 60% of its initial specific capacity after 3000 GCD cycles (Figure 13d). A factor that can influence the loss of capacitance retention may be the fact that when the residual amount of ethanol used in the PVP solution that remains in the solid electrolyte is lost, the ionic conductivity of the PVP-$LiClO_4$ solid electrolyte decreases [33].

After 300 CV cycles, the electrodes of the SSC were recovered and washed with ethanol to remove the electrolyte on the electrode surface. SEM images (Figure 14a) of the electrode after 300 CV cycles with anodic conditions at the end of the last CV cycle show a more textured surface than the original electrode surface (Figure 3a). SEM-EDS images (Figure 14b,c) show a homogeneous distribution of Mn and Zn on the electrode surface, the same as the TEM-EDS image of the cross-section (Figure 14d,f).

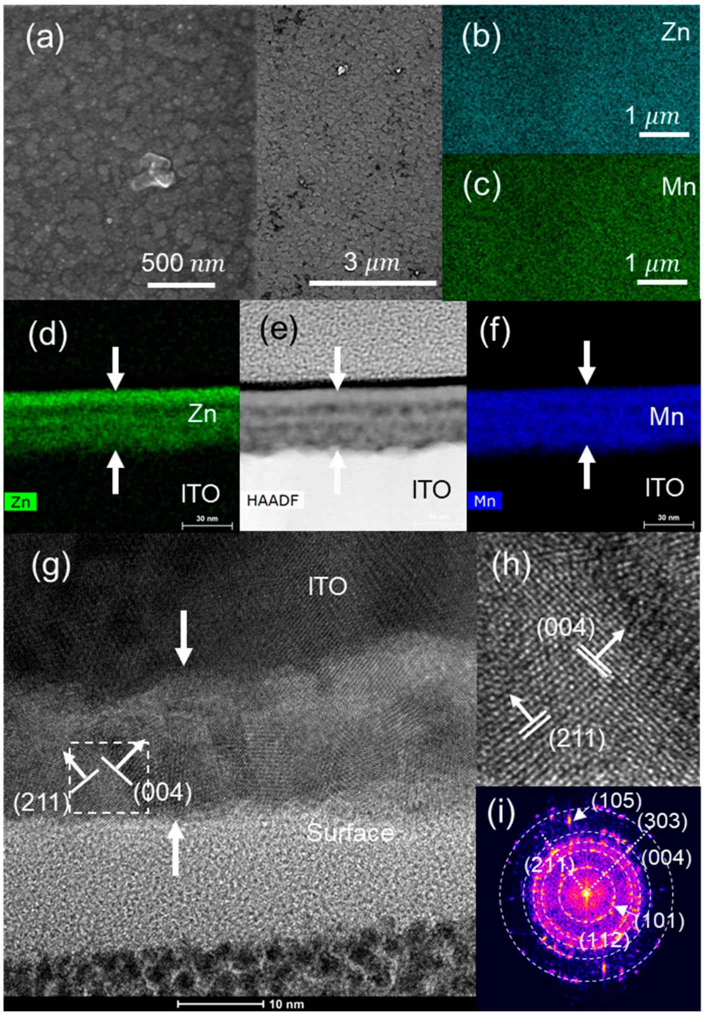

Figure 14. SCC with PVP-$LiClO_4$ as electrolyte after 300 CV cycles: (**a**) SEM; (**b**) Zn and (**c**) Mn EDS images of the surface of the electrode; (**d**) Zn and (**f**) Mn EDS images; (**e**) HAADF images of the electrode cross-section; (**g**) HRTEM image of the cross-section; (**h**) magnification of the marked zone; (**i**) FFT of the film cross-section.

The XPS Zn2p (Figure 15a) and the ZnLMM spectra (Figure 15b) are similar to those of the corresponding original spinel surface. The Mn2p and M3s-Zn3p peaks are also similar to those of the $ZnMn_2O_4$ spinel. After the 300th CV cycle, the $Mn2p_{3/2}$ region of the electrode finished in cathodic conditions shows a very slight contribution to lower binding energy, 0.2 eV, corresponding to the presence of reduced Mn valences (Figure 15d). The XPS spectra of the Zn2p, ZnLMM, and Zn3p-Mn3s regions of the electrode after 300 cycles of CV are very similar to those obtained for the electrode before CV. If we compare this with what occurred with the other two electrolytes, the $ZnMn_2O_4$ spinel in the SCC with PVP-$LiClO_4$ was shown to be more stable after 300 CV cycles. Using the fast Fourier-transform (FFT) HRTEM of the cross-section (Figure 14g,h), it is possible to identify crystalline planes compatibles with a mix of spinel $ZnMn_2O_4$ (PDF 01-071-2499) and Mn-rich tetragonal phases, such as $Zn_{0,75}Mn_{2,25}O_4$ (PDF 04-016-9607), with a stoichiometry change across the cross-section (Figure S8). In this case, due to the fact that Zn^{2+} has a similar ionic radius (0.74 Å) to that of Li^+ (0.76 Å), the intercalation of Li^+ into the spinel structure could play a role in the faradaic processes [69].

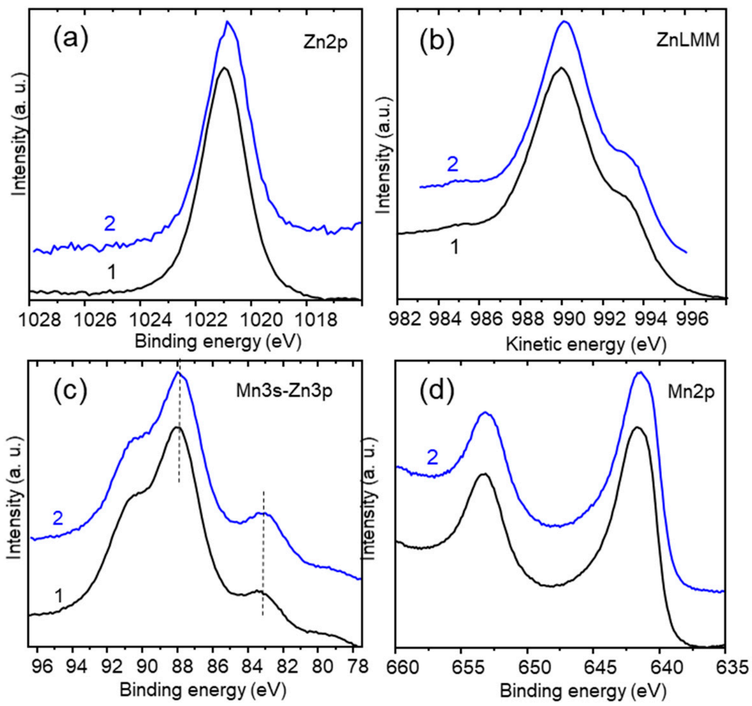

Figure 15. XPS of electrode of SCC PVP-$LiClO_4$: (**a**) Zn2p, (**b**) ZnLMM, (**c**) M3s Zn3p, (**d**) Mn2p. Electrodes: (1) as-deposited, (2) after 300 CV cycles finishing under reducing conditions.

Figure 16 shows the Ragone plot at 0.5 A g^{-1}, 1.0 A g^{-1}, and 2.0 A g^{-1} for the three SCC_S. All of them showed supercapacitor behavior.

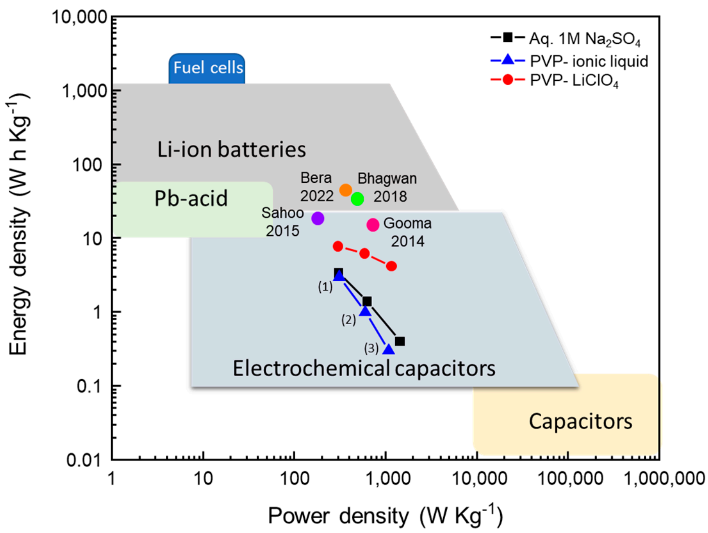

Figure 16. Ragone plot, points corresponding to (1) 0.5 A g^{-1}, (2) 1.0 A g^{-1}, (3) 2.0 A g^{-1}, and values obtained by other authors [70–73].

4. Conclusions

$ZnMn_2O_4$ thin films were prepared using the spray pyrolysis method and used as transparent electrodes in symmetric supercapacitors. The electrical resistivity of the films limited the film thickness of $ZnMn_2O_4$. $ZnMn_2O_4$ thin films were tested in a three-electrode electrochemical cell with aqueous 1.0 M Na_2SO_4 as the electrolyte, showing a specific capacity of 697 F g^{-1} and a specific capacity retention of 70% after 3000 GCD cycles. The challenge remains to ensure that the specific capacitance obtained with the three-electrode electrochemical cell does not decrease when the electrode is used in the supercapacitor.

Of the three electrolytes tested, the SCC with 1.0 M Na_2SO_4 showed the best specific capacitance, but also showed the lowest capacitance retention due to irreversible Zn loss and corrosion of the active electrode material. PVP-ionic liquid and PVP-$LiClO_4$ electrolytes preserve the tetragonal spinel structure of the electrode with changes in stoichiometry to a Mn-rich $Zn_{1-x}M_{3-x}O_4$, which can be interpreted as a semi-reversible process of Zn^{2+} deintercalation/intercalation without evidence of a loss of active electrode material along the CV cycles. In the case of the electrolyte 1.0 M Na_2SO_4, the loss of Zn^{2+} leads to the formation of MnO_2 via $Zn_{1-x}M_{3-x}O_4$. XPS analysis of the two electrodes forming the symmetric supercapacitor shows that there is a change in the Mn valence on the electrode surface, with the presence of Mn^{4+} or Mn^{2+} depending on if, at the end of the final cycle, the electrode was exposed to more oxidizing or reducing conditions. It is observed in the SCC PVP-ionic liquid that, on the electrode surface, there is an interaction between the anion $[BF_4^-]$ of the ionic liquid and the Zn^{2+}. The Ragone plot (Figure 16) of the three SSCs shows supercapacitor behavior; pseudocapacitance is the main contributor. The electrochemical results prove that pseudocapacitance is the major contributor to the electrode capacitance and that SCCs can therefore be considered as pseudocapacitors.

Supplementary Materials: The following supporting information can be downloaded at https://www.mdpi.com/article/10.3390/nano13233017/s1; Figure S1: Three-electrode cyclic voltammogram curves at different scan rates: 5, 10, 25, 50, 75, 100, 150, and 200 mV s^{-1}; Table S1: Values of specific capacitance obtained by different authors; Figure S2: Example of EDS spectrum of the $ZnMn_2O_4$ electrode as obtained, and atomic percentages of Mn and Zn; Figure S3: Example of EDS spectrum of the electrode after 3000 CV cycles and local values of the atomic percentage of the different chemical elements; Figure S4: Cyclic voltammetry curves of SSC assembled with 1.0 M Na_2SO_4. (a) ±0.4 V; (b) ±0.8 V; (c) ±1.2 V; (d) ±1.5 V with different scan rates: 25 mV s^{-1}, 50 mV s^{-1}, 75 mV s^{-1}, 100 mV s^{-1}, 150 mV s^{-1}, and 200 mV s^{-1}; Table S2: (a) Specific capacitance, energy, and power density calculated from cyclic voltammetry; (b) GCD measurements of the SSC assembled with 1.0 M Na_2SO_4 electrolyte; Figure S5: Cyclic voltammetry curves of SSC assembled with PVP-ionic liquid. (a) ±0.4 V; (b) ±0.8 V; (c) ±1.2 V; (d) ±1.5 V with different scan rates: 25 mV s^{-1}, 50 mV s^{-1}, 75 mV s^{-1}, 100 mV s^{-1}, 150 mV s^{-1}, and 200 mV s^{-1}; Table S3: (a) Specific capacitance, energy, and power density calculated from cyclic voltammetry and (b) GCD measurements of the SSC assembled with PVP-ionic liquid; Figure S6: (a) HAADF image EDS of the cross-section of the SCC (PVP-ionic liquid) electrode after 300 CV cycles; (b) Mn/Zn atomic ratio and (c) atomic percentages of Mn and Zn, along the line marked on the HAADF image; Figure S7: Cyclic voltammetry curves of SSC assembled with PVP-ionic liquid. (a) ±0.4 V; (b) ±0.8 V; (c) ±1.2 V; (d) ±1.5 V with different scan rates: 25 mV s^{-1}, 50 mV s^{-1}, 75 mV s^{-1}, 100 mV s^{-1}, 150 mV s^{-1}, and 200 mV s^{-1}; Table S4: (a) Specific capacitance, energy, and power density calculated from cyclic voltammetry; (b) galvanostatic charge–discharge measurements of the SSC assembled with PVP-$LiClO_4$; Table S5: (a) Specific capacitance, energy and power density calculated from cyclic voltammetry; (b) galvanostatic charge-discharge measurements of the SSC assembled with PVP-$LiClO_4$; Figure S8: (a) HAADF image EDS of the cross-section of the SCC electrode (PVP-$LiClO_4$) after 300 CV cycles; (b) Mn/Zn atomic ratio; and (c) atomic percentages of Mn and Zn, along the line marked on the HAADF image; Figure S9: (a) SEM images of the surface of the electrode as obtained. SEM images of the surface of the SSC electrode after 300 CV cycles using as electrolyte: (b) 1.0 M Na_2SO4, (c) PVP-ionic liquid, and (d) PVP-$LiClO_4$ [2,45,70,74–78].

Author Contributions: J.J.P.-P., Methodology, Investigation, Formal Analysis, Validation, Writing; M.C.L.-E., Methodology, Investigation, Supervision, Review; F.M., Conceptualization, Formal Analysis, Validation, Resources, Writing—Review and Editing, Visualization, Supervision, Project Administration, Funding Acquisition. All authors have read and agreed to the published version of the manuscript.

Funding: This research was financed by project PID2020–117832RB-100 (MCIN/AEI/10.13039/501100011033), Spain.

Data Availability Statement: The data presented in this study are available upon request from the corresponding author.

Conflicts of Interest: The authors declare no conflict of interest.

References

1. Winter, M.; Brodd, R.J. What Are Batteries, Fuel Cells, and Supercapacitors? *Chem. Rev.* **2004**, *104*, 4245–4270. [CrossRef] [PubMed]
2. Abdollahifar, M.; Huang, S.S.; Lin, Y.H.; Li, Y.C.; Shih, B.Y.; Sheu, H.S.; Liao, Y.F.; Wu, N.I. High-performance carbon-coated $ZnMn_2O_4$ nanocrystallite supercapacitors with tailored microstructures enabled by a novel solution combustion method. *J. Power Sources* **2018**, *378*, 90–97. [CrossRef]
3. Simon, P.; Gogotsi, Y. Materials for Electrochemical Capacitors. *Nat. Mater.* **2008**, *7*, 845–854. [CrossRef] [PubMed]
4. Yuan, Y.; Zhu, J.; Wang, Y.; Li, S.; Jin, P.; Chen, Y. Facile synthesis of manganese oxide nanostructures with different crystallographic phase and morphology for supercapacitors. *J. Alloys Compd.* **2020**, *830*, 154524. [CrossRef]
5. Chen, S.; Xing, W.; Duan, J.; Hu, X.; Qiao, S.Z. Nanostructured morphology control for efficient supercapacitor electrodes. *J. Mater. Chem. A* **2013**, *1*, 2941–2954. [CrossRef]
6. Ma, R.; Wang, M.; Dam, D.T.; Yoon, Y.J.; Chen, Y.; Lee, J.M. Polyaniline-coated hollow Fe_2O_3 nanoellipsoids as an anode material for high-performance lithium-ion batteries. *ChemElectroChem* **2015**, *2*, 503–507. [CrossRef]
7. Ma, R.; Zhou, Y.; Yao, L.; Liu, G.; Zhou, Z.; Lee, J.M.; Wang, J.; Liu, Q. Capacitive behaviour of MnF_2 and CoF_2 submicro/nanoparticles synthesized via a mild ionic liquid-assisted route. *J. Power Sources* **2016**, *303*, 49–56. [CrossRef]
8. Zhang, Q.; Feng, L.; Liu, Z.; Jiang, L.; Lan, T.; Zhang, C.; Liu, K.; He, S. High Rate Performance Supercapacitors Based on N, O Co-Doped Hierarchical Porous Carbon Foams Synthesized via Chemical Blowing and Dual Templates. *Molecules* **2023**, *28*, 6994. [CrossRef]
9. Yan, B.; Zhao, W.; Zhang, Q.; Kong, Q.; Chen, G.; Zhang, C.; Han, J.; Jiang, S.; He, S. One stone for four birds: A "chemical blowing" strategy to synthesis wood-derived carbon monoliths for high-mass loading capacitive energy storage in low temperature. *J. Colloid Interface Sci.* **2024**, *653*, 1526–1538. [CrossRef]
10. Dhandapani, E.; Thangarasu, S.; Ramesh, S.; Ramesh, K.; Vasudevan, R.; Duraisamy, N. Recent development and prospective of carbonaceous material, conducting polymer and their composite electrode materials for supercapacitor—A review. *J. Energy Storage* **2022**, *52*, 104937. [CrossRef]
11. An, C.; Zhang, Y.; Guo, H.; Wang, Y. Metal oxide-based supercapacitors: Progress and prospective. *Nanoscale Adv.* **2019**, *1*, 4644–4658. [CrossRef] [PubMed]
12. Wu, Z.S.; Zhou, G.; Yin, L.C.; Ren, W.; Li, F.; Cheng, H.M. Graphene/metal oxide composite electrode materials for energy storage. *Nano Energy* **2012**, *1*, 107–131. [CrossRef]
13. Huang, M.; Zhang, Y.; Li, F.; Zhang, L.; Ruoff, R.S.; Wen, Z.; Liu, Q. Self-Assembly of Mesoporous Nanotubes Assembled from Interwoven Ultrathin Birnessite-Type MnO_2 nanosheets for Asymmetric Supercapacitors. *Sci. Rep.* **2014**, *4*, 3879. [CrossRef]
14. Lee, H.Y.; Goodenough, J.B. Supercapacitor Behavior with KCl Electrolyte. *J. Solid State Chem.* **1999**, *14*, 220–223. [CrossRef]
15. Post, J.E. Manganese oxide minerals: Crystal structures and economic and environmental significance. *Proc. Natl. Acad. Sci. USA* **1999**, *96*, 3447–3454. [CrossRef] [PubMed]
16. Ilton, E.S.; Post, E.; Heaney, P.J.; Ling, F.T.; Kerisit, S.N. XPS determination of Mn oxidation states in Mn (hydr)oxides. *Appl. Surf. Sci.* **2016**, *366*, 475–485. [CrossRef]
17. Ghost, S.K. Diversity in the Family of Manganese Oxides at the Nanoscale: From Fundamentals to Applications. *ACS Omega* **2020**, *5*, 25493–25504. [CrossRef]
18. Sun, P.; Yi, H.; Peng, T.; Jing, Y.; Wang, R.; Wang, H.; Wang, X. Ultrathin MnO_2 nanoflakes deposited on carbon nanotube networks for symmetrical supercapacitors with enhanced performance. *J. Power Sources* **2017**, *341*, 27–35. [CrossRef]
19. Weng, Y.T.; Pan, H.A.; Lee, R.C.; Huang, T.Y.; Chu, Y.; Lee, J.F.; Sheu, H.S. Spatially confined MnO_2 nanostructure enabling consecutive reversible charge transfer from Mn(IV) to Mn(II) in a mixed pseudocapacitor-battery electrode. *Adv. Energy Mater.* **2015**, *5*, 1500772. [CrossRef]
20. Knight, C.J.; Soosairaj, T.; Manthiram, A. Chemical Extraction of Zn from $ZnMn_2O_4$-based spinels. *J. Mater. Chem. A* **2015**, *3*, 21077. [CrossRef]
21. Kang, L.; Huang, C.; Zhang, J.; Zhang, M.; Zhang, N.; He, Y.; Luo, C.; Wang, C.; Zhou, X.; Wu, X. A new strategy for synthesis of hierarchical MnO_2-Mn_3O_4 nanocomposite via reduction-induced exfoliation of MnO_2 nanowires and its application in high-performance asymmetric supercapacitor. *Compos. Part B Eng.* **2019**, *177*, 107501. [CrossRef]
22. Rubel, O.; Tran, T.N.T.; Gourley, S. Electrochemical Stability of $ZnMn_2O_4$: Understanding Zn-Ion Rechargeable Battery Capacity and Degradation. *J. Phys. Chem. C* **2022**, *126*, 10957–10967. [CrossRef]
23. Deng, W.; Xu, Y.; Zhang, X.; Li, C.; Liu, Y.; Xiang, K.; Chen, H. $(NH_4)_2Co_2V_{10}O_{28}\cdot16H_2O/(NH_4)_2V_{10}O_{25}\cdot8H_2O$ heterostructure as cathode for high-performance aqueous Zn-ion batteries. *J. Alloys Compd.* **2022**, *903*, 163824. [CrossRef]
24. Nádherný, L.; Maryško, M.; Sedmidubský, D.; Martin, C. Structural and magnetic properties of $ZnxMn_3$-xO_4 spinels. *J. Magn. Magn. Mater.* **2016**, *413*, 89–96. [CrossRef]
25. Dang, W.; Wang, F.; Ding, Y.; Feng, C.; Guo, Z. Synthesis and electrochemical properties of $ZnMn_2O_4$ microspheres for lithium-ion battery application. *J. Alloys Compd.* **2017**, *690*, 72–79. [CrossRef]

26. Ivanova, I.V.; Zaitseva, N.A.; Samigullina, R.F.; Krasnenko, T.I. Solid-state synthesis of $ZnMn_2O_4$ spinel: Sequence of phase transformations, thermal stability, localization and charge state of manganese ions in the intermediate and final reaction products. *Solid State Sci.* **2023**, *136*, 107110. [CrossRef]
27. Driessens, F.C.M.; Rieck, G.D. Phase equilibria in the system Zn-Mn-O in air. *J. Inorg. Nucl. Chem.* **1966**, *28*, 1593–1600. [CrossRef]
28. Peiteado, M.; Sturm, S.; Caballero, A.C.; Makovec, D. Mn_3-xZnxO_4 spinel phases in the Zn-Mn-O system. *Acta Mater.* **2008**, *56*, 4028–4035. [CrossRef]
29. Zhao, Z.; Tian, G.; Sarapulova, A.; Trouillet, V.; Fu, Q.; Geckle, U.; Ehrenberg, H.; Dsoke, S. Elucidating the energy storage mechanism of $ZnMn_2O_4$ as promising anode for Li-ion batteries. *J. Mater. Chem. A* **2018**, *6*, 19381. [CrossRef]
30. Zhang, L.; Zhu, S.; Cao, H.; Pang, G.; Lin, J.; Hou, L.; Yuan, F. Ultrafast spray pyrolysis fabrication of a nanophase $ZnMn_2O_4$ anode towards high-performance Li-ion batteries. *RSC Adv.* **2015**, *15*, 13667–13673. [CrossRef]
31. Saranya, P.E.; Selladurai, S. Efficient electrochemical performance of $ZnMn_2O_4$ nanoparticles with rGO nanosheets for electrodes in supercapacitor applications. *J. Mater. Sci. Mater. Electron.* **2018**, *29*, 3326–3339. [CrossRef]
32. Rodríguez, J.; Navarrete, E.; Dalchiele, E.A.; Sánchez, L.; Ramos-Barrado, J.R.; Martín, F. Polyvinylpyrrolidonee-$LiClO_4$ solid polymer electrolyte and its application in transparent thin film supercapacitors. *J. Power Sources* **2013**, *237*, 270–276. [CrossRef]
33. Astorga, E.N.; Rodríguez, J.; Dalchiele, E.A.; Schrebler, R.; Leyton, P.; Ramos-Barrado, J.R.; Martín, F. A transparent solid-state ion gel for supercapacitor device applications. *J. Solid State Electrochem.* **2017**, *21*, 1431–1444. [CrossRef]
34. Heiba, Z.K.; Mohamed, M.B.; Ahmed, S.I. Modifying the structure and optical characteristics of $1ZnMn_2O_4$ by alloying with CdS to form heterostructure nanocomposite. *Appl. Phys. A* **2021**, *127*, 883. [CrossRef]
35. Heiba, Z.K.; Ghannam, M.M.; Sanad, M.M.S.; Albassam, A.A.; Mohamed, M.B. Structural, optical, and dielectric properties of nano-$ZnMn_2-$xVxO_4. *J. Mater. Sci. Mater. Electron.* **2020**, *31*, 8946–8962. [CrossRef]
36. Zhang, T.; Yue, H.J.; Qiu, H.L.; Zhu, K.; Zhang, L.J.; Wei, Y.J.; Du, F.; Chen, G.; Zhang, D. Synthesis of graphene-wrapped $ZnMn_2O_4$ hollow microspheres as high performance anode materials for lithium ion batteries. *RSC Adv.* **2015**, *5*, 99107–99114. [CrossRef]
37. Tian, Y.; Chen, Z.; Tang, W.; Yang, Z.; Zhang, W.; Li, S.; Wang, K.; Sun, Y.; Xia, Q.; Guo, B. A facile synthetic protocol to construct 1D Zn-Mn-Oxide nanostructures with tunable compositions for high-performance lithium storage. *J. Alloys Compd.* **2017**, *720*, 376–382. [CrossRef]
38. Aouini, S.; Bardaoui, A.; Ferraria, A.M.; Santos, D.M.F.; Chtourou, R. $ZnMn_2O_4$ Nanopyramids Fabrication by Hydrothermal Route: Effect of Reaction Time on the Structural, Morphological, and Electrochemical Properties. *Energies* **2022**, *15*, 9352. [CrossRef]
39. Minelli, A.; Dolcet, P.; Diodati, S.; Gardonio, S.; Innocenti, C.; Badocco, D.; Gialanella, S.; Pastore, P.; Pandolfo, L.; Caneschi, A.; et al. Pursuing the stabilisation of crystalline nanostructured magnetic manganites through a green low temperature hydrothermal synthesis. *J. Mater. Chem. C* **2017**, *5*, 3359–3371. [CrossRef]
40. Fujiwara, M.; Matsushita, T.; Ikeda, S. Evaluation of Mn3s X-ray photoelectron spectroscopy for characterization of manganese complexes. *J. Electron. Spectrosc. Relat. Phenom.* **1995**, *74*, 201–206. [CrossRef]
41. Lei, K.; Han, X.; Hu, Y.; Liu, X.; Cong, L.; Cheng, F. Chemical etching of manganese oxides for electrocatalytic oxygen reduction reaction. *Chem. Commun.* **2015**, *51*, 11599. [CrossRef]
42. Toupin, M.; Brousse, T.; Belanger, D. Charge Storage Mechanism of MnO_2 Electrode Used in Aqueous Electrochemical Capacitor. *Chem. Mater.* **2004**, *16*, 3184–3190. [CrossRef]
43. Beyreuther, E.; Grafström, S.; Eng, L.M.; Thiele, C.; Dörr, K. XPS investigation of Mn valence in lanthanum manganite thin films under variation of oxygen. *Phys. Rev. B* **2006**, *73*, 155425. [CrossRef]
44. Boukmouche, N.; Azzouz, N.; Bouchama, L.; Daltin, A.L.; Chopart, J.P.; Bouznit, Y. Supercapacitance of MnO_2 films Prepared by Pneumatic Spray Method. *Mater. Sci. Semicond. Process.* **2014**, *27*, 233–239. [CrossRef]
45. Guo, N.; Wei, X.; Deng, X.L.; Xu, X.J. Synthesis and Property of Spinel Porous $ZnMn_2O_4$ microspheres. *Appl. Surf. Sci.* **2015**, *356*, 1127–1134. [CrossRef]
46. Tanggarnjanavalukul, C.; Phattharasupakun, N.; Wutthiprom, J.; Kidkhunthod, P.; Sawangphruk, M. Charge storage mechanisms of birnessite-type MnO_2 nanosheets in Na_2SO_4 electrolytes with different pH values: In situ electrochemical X-ray absorption spectroscopy investigation. *Electrochim. Acta* **2018**, *273*, 17–25. [CrossRef]
47. Dubal, D.; Dhawale, D.; Salunkhe, R.; Pawar, S.; Lokhande, C. A Novel Chemical Synthesis and Characterization of Mn_3O_4 Thin Films for Supercapacitor Application. *Appl. Surf. Sci.* **2010**, *256*, 4411–4416. [CrossRef]
48. Sankar, K.V.; Kalpana, D.; Selvan, R.K. Electrochemical Properties of Microwave-Assisted Reflux-Synthesized Mn_3O_4 Nanoparticles in Different Electrolytes for Supercapacitor Applications. *J. Appl. Electrochem.* **2012**, *42*, 463–470. [CrossRef]
49. Pan, H.; Shao, Y.; Yan, P.; Cheng, Y.; Han, K.S.; Nie, Z.; Wang, C.; Yang, J.; Li, X.; Bhattacharya, P.; et al. Reversible aqueous zinc/manganese oxide energy storage from conversion reactions. *Nat. Energy* **2016**, *1*, 16039. [CrossRef]
50. Zhao, X.; Hou, Y.; Wang, Y.; Yang, L.; Zhu, L.; Cao, R.; Sha, Z. Prepared MnO_2 with different crystal forms as electrode materials for supercapacitors: Experimental research from hydrothermal crystallization process to electrochemical performances. *RSC Adv.* **2017**, *7*, 40286. [CrossRef]
51. Shan, X.; Abeykoon, A.M. Framwork Doping of Ni Enhances Pseudocapacite Na-ion storage of Ni(MnO_2) layered Birnessite. *Chem. Mater.* **2019**, *31*, 8774–8786. [CrossRef]

52. Chen, L.; Yang, Z.; Qin, H.; Zeng, X.; Meng, J. Advanced electrochemical performance of $ZnMn_2O_4$/N-doped graphene hybrid as cathode material for zinc battery. *J. Powers Sources* **2019**, *425*, 162–169. [CrossRef]
53. Zhang, N.; Cheng, F.; Liu, J.; Wang, L.; Long, X.; Liu, X.; Li, F.; Chen, J. Rechargeable aqueous zinc-manganese dioxide batteries with high energy and power densities. *Nat. Commun.* **2017**, *8*, 405. [CrossRef]
54. Dong, R.; Ye, Q.; Kuang, L.; Lu, X.; Zhang, Y.; Zhang, X.; Tan, G.; Wen, Y.; Wang, F. Enhanced Supercapacitor Performance of Mn_3O_4 Nanocrystals by Doping Transition-Metal Ions. *ACS Appl. Mater. Interfaces* **2013**, *5*, 9508–9516. [CrossRef] [PubMed]
55. Sankar, K.V.; Surendran, S.; Pandi, K.; Allin, A.M.; Nithya, V.D.; Lee, Y.S.; Kafai Selvan, R. Studies on the electrochemical intercalation/de-intercalation mechanism of $NiMn_2O_4$ for high stable pseudocapacitor electrodes. *RSC Adv.* **2015**, *5*, 27649–27656. [CrossRef]
56. Chavan, U.J. Electrochemical behavior of spray deposited mixed nickel mangase oxide thin films for supercapacitor applications. *J. Mater. Sci. Mater. Electron.* **2017**, *28*, 4958–4964. [CrossRef]
57. Singh, A.; Chandra, A. Significant Performance Enhancement in Asymmetric Supercapacitors based on Metal Oxides, Carbon nanotubes and Neutral Aqueous Electrolyte. *Sci. Rep.* **2015**, *5*, 15551. [CrossRef]
58. Wen, X.; Luo, J.; Xiang, K.; Zhou, W.; Zhang, C.; Chen, H.J. High-performance monoclinic WO_3 nanospheres with the novel NH^{4+} diffusion behaviors for aqueous ammonium-ion batteries. *Chem. Eng.* **2023**, *458*, 141381. [CrossRef]
59. Marveh, F.; Scott, W.D. Method Comparison for Deconvoluting Capacitive and Pseudo-Capacitive Contributions to Electrochemical Capacitor Electrode Behavior. *J. Electrochem. Soc.* **2018**, *165*, A664–A673. [CrossRef]
60. Basant, A.A.; Asma, M.A.O.; Ahmed, S.G.K.; Nageh, K. Untapped, Potential of Polymorph MoS_2: Tuned Cationic Intercalation for High-Performance Symmetric Supercapacitors. *ACS Appl. Mater. Interfaces* **2019**, *11*, 33955–33965. [CrossRef]
61. Sathiya, M.; Prakash, A.S.; Ramesha, K.; Tarascon, J.M.; Shukla, A.K. V_2O_5, Anchored Carbon Nanotubes for Enhanced Electrochemical Energy Storage. *J. Am. Chem. Soc.* **2011**, *133*, 16291–16299. [CrossRef] [PubMed]
62. Wang, J.; Polleux, J.; Lim, J.; Dunn, B. Pseudocapacitive Contributions to Electrochemical Energy Storage in TiO_2 (Anatase) Nanoparticles. *J. Phys. Chem. C* **2007**, *111*, 14925–14931. [CrossRef]
63. Iamprasertkun, P.; Tanggarnjanavalukul, C.; Krittayavathananon, A.; Khuntilo, J.; Chanlek, N.; Kidkhunthod, P.; Sawangphruk, M. Insight into charge storage mechanisms of layered MnO_2 nanosheets for supercapacitor electrodes: In situ electrochemical X-ray absorption spectroscopy. *Electrochim. Acta* **2017**, *249*, 26–32. [CrossRef]
64. Zhang, N.; Cheng, F.; Liu, Y.; Zhao, Q.; Lei, K.; Chen, C.; Liu, X.; Chen, J. Cation-Deficient Spinel $ZnMn_2O_4$ cathode in $Zn(CF_3SO_3)$ electrolyte for rechargeable aqueous Zn-Ion Battery. *J. Am. Chem. Soc.* **2016**, *138*, 12894–12901. [CrossRef] [PubMed]
65. Di Castro, V.; Polzonetti, G. XPS Study of Mn oxidation. *J. Electron Spectros. Relat. Phenom.* **1989**, *48*, 117–123. [CrossRef]
66. Ardizzone, S.; Bianchi, C.L.; Tirelli, D. Mn_3O_4 and γ-MnOOH powders, preparation, phase composition and XPS characterisation. *Colloids Surf. A Physicochem. Eng. Asp.* **1998**, *134*, 305–312. [CrossRef]
67. Liu, Y.; Wu, X. Strategies for constructing manganese-based oxide electrode materials for aqueous rechargeable zinc-ion batteries. *Chin. Chem. Lett.* **2022**, *33*, 1236–1244. [CrossRef]
68. Moulder, J.F.; Stickle, W.F.; Sobol, P.E.; Bomben, K.D. *Handbook of X-ray Photoelectron Spectroscopy*; Physical Electronics Inc.: Eden Prairie, MN, USA, 1992.
69. Liu, H.; Wang, J.G.; You, Z.; Wei, C.; Kang, F.; Wei, B. Rechargeable aqueous zinc-ion batteries: Mechanism, design strategies and future perspectives. *Mater. Today* **2021**, *42*, 73–98. [CrossRef]
70. Sahoo, A.; Sharma, Y. Synthesis and characterization of nanostructured ternary zinc manganese oxide as novel supercapacitor material. *Mater. Chem. Phys.* **2015**, *149–150*, 721–727. [CrossRef]
71. Bhagwan, J.; Kumar, N.; Yadav, K.L.; Sharma, Y. Probing the electrical properties and energy storage performance of electrospun $ZnMn_2O_4$ nanofibers. *Solid State Ion.* **2018**, *321*, 75–82. [CrossRef]
72. Bera, A.; Halder, L.; Si, S.K.; De, A.; Ojha, S.; Bera, S.; Maity, P.; Mondal, A.; Khatua, B.B. Fabrication of a flexible quasi-solid-state asymmetric supercapacitor device based on a spherical honeycomb like $ZnMn_2O_4@Ni(OH)_2$ hybrid core-shell electrode material with superior electrochemical performances. *Results Chem.* **2022**, *4*, 100404. [CrossRef]
73. Gooma, A.M.; Ling, L.T.; Rajan, J.; Mashitah, M.Y.; Kwok, F.C. Electrochemical performance studies of MnO_2 nanoflowers recovered from spent battery. *Mater. Res. Bull.* **2014**, *60*, 5–9. [CrossRef]
74. Senthilkumar, N.; Venkatachalam, V.; Kandiban, M.; Vigneshwaran, P.; Jayavel, R.; Potheher, I.V. Studies on Electrochemical Properties of Hetarolite ($ZnMn_2O_4$) Nanostructure for Supercapacitor Application. *Phys. E Low-Dimens. Syst. Nanostruct.* **2019**, *106*, 121–126. [CrossRef]
75. Aruchamy, K.; Nagaraj, R.; Manohara, H.M.; Nidhi, M.R.; Mondal, D.; Ghosh, D.; Nataraj, K. One-step green route synthesis of spinel $ZnMn_2O_4$ nanoparticles decorated on MWCNTs as a novel electrode material for supercapacitor. *Mater. Sci. Eng. B* **2020**, *252*, 114481. [CrossRef]
76. Wei, X.Q.; Wang, Y.L.; Guo, N.; Deng, X.; Xu, X.J. Effect of growing temperature on structure and electrochemical performance of $ZnMn_2O_4$ nanospheres. *Ionics* **2017**, *23*, 2443–2448. [CrossRef]

77. Mani, M.P.; Venkatachalam, V.; Thamizharasan, K.; Jothibas, M. Evaluation of Cubic-Like Advanced $ZnMn_2O_4$ Electrode for High-Performance Supercapacitor Applications. *J. Electron. Mater.* **2021**, *50*, 4381–4387. [CrossRef]
78. Sannasi, V.; Subbian, K. A facile synthesis of $ZnMn_2O_4/Mn_2O_3$ composite nanostructures for supercapacitor applications. *Ceram. Int.* **2021**, *47*, 12300–12309. [CrossRef]